The Astrophysical Journal, 859:66 (20pp), 2018 May 20 https://doi.org/10.3847/1538-4357/aabfc3

Delayed Shock-induced Dust Formation in the Dense Circumstellar Shell Surrounding the Type IIn Supernova SN 2010jl

Arkaprabha Sarangi[1], Eli Dwek, and Richard G. Arendt[2]
Observational Cosmology Lab, NASA Goddard Space Flight Center, Mail Code 665, Greenbelt, MD 20771, USA; arkaprabha.sarangi@nasa.gov, eli.dwek@nasa.gov
Received 2018 February 23; revised 2018 April 17; accepted 2018 April 18; published 2018 May 24

Abstract

The light curves of Type IIn supernovae are dominated by the radiative energy released through the interaction of the supernova shock waves with their dense circumstellar medium (CSM). The ultraluminous Type IIn supernova SN 2010jl exhibits an infrared emission component that is in excess of the extrapolated UV–optical spectrum as early as few weeks postexplosion. This emission has been considered by some as evidence for the rapid formation of dust in the cooling postshock CSM. We investigate the physical processes that may inhibit or facilitate the formation of dust in the CSM. When only radiative cooling is considered, the temperature of the dense shocked gas rapidly drops below the dust condensation temperature. However, by accounting for the heating of the postshock gas by the downstream radiation from the shock, we show that dust formation is inhibited until the radiation from the shock weakens as it propagates into the less dense outer regions of the CSM. In SN 2010jl, dust formation can therefore only commence after day ∼380. Only the IR emission since that epoch can be attributed to the newly formed CSM dust. Observations on day 460 and later show that the IR luminosity exceeds the UV–optical luminosity. The postshock dust cannot extinct the radiation emitted by the expanding SN shock. Therefore, its IR emission must be powered by an interior source, which we identify as the reverse shock propagating through the SN ejecta. IR emission before day 380 must therefore be an IR echo from preexisting CSM dust.

Key words: circumstellar matter – dust, extinction – infrared: stars – shock waves – supernovae: general – supernovae: individual (SN 2010jl)

1. Introduction

Core-collapse supernovae (CCSNe) are the final fate of massive stars larger than 8 $M_{\odot}$ at the main sequence. They play a significant role in the chemical enrichment of the host galaxy through the synthesis of metals and dust. Prior to the explosion, the progenitor stars undergo phases of mass loss in the form of winds. In most cases, the mass-loss rates are estimated to vary between 10^{-7} and 10^{-4} $M_{\odot}$ yr^{-1} depending on the metallicity and the mass (Meynet et al. 2015). However, in the case of some progenitors, the mass-loss rate can be $>10^{-2}$ $M_{\odot}$ (Kiewe et al. 2012; Moriya et al. 2014), leading to the formation of a dense circumstellar medium (CSM) surrounding the preexplosion star (Chugai & Danziger 1994). Despite being only a small fraction (<10%) of all observed CCSNe, the unique features of Type IIn supernovae (SNe) help us understand important aspects of the pre- and postexplosion phases in massive stars (Fassia et al. 2001; Chugai & Danziger 2003; Fox et al. 2011; Whalen et al. 2013).

The transfer of radiative energy through the surrounding medium enables us to understand the nature of the progenitor, the explosion, and the properties of the CSM (Chugai et al. 2004; Dessart & Hillier 2010). Depending on the shape of their light curve and spectral type, CCSNe have been categorized into several subclasses (Filippenko 1997). Type IIn SNe, introduced by Schlegel (1990), are characterized by the presence of narrow (∼100 km s^{-1}), intermediate (1–4 × 10^3 km s^{-1}), and broad (10–15 × 10^3 km s^{-1}) velocity width components. The narrow component originates from the slow-moving CSM before being traversed by the SN shock; the source of the intermediate-width component is the postshock region of the CSM, whereas the broad component arises from fast-expanding SN ejecta (Smith et al. 2008).

Of the Type IIn SNe that have been observed over the last decade (Taddia et al. 2013), SN 2010jl in UGC 5189 (Stoll et al. 2011) has been extensively probed at X-ray wavelengths with the the *Chandra*, *NuSTAR*, and *Swift* satellites (Ofek et al. 2014a; Chandra et al. 2015), and at UV, optical, and near-IR wavelengths with the *Hubble Space Telescope* (*HST*), the VLT/X and Subaru observatories, and the *Spitzer* satellite (Maeda et al. 2013; Fransson et al. 2014; Gall et al. 2014). The observations have provided important information on the progenitor mass, and the composition and morphology of its circumstellar environment (Andrews et al. 2011a; Fox et al. 2013; Williams & Fox 2015; Fox et al. 2017).

The luminosity of the UV–optical (UVO) light curve of SN 2010jl is characterized by a slow $t^{-0.4}$ decline from an initially observed value of $L \sim 4 \times 10^9$ $L_{\odot}$ on day 20 to a value of $\sim 2 \times 10^9$ $L_{\odot}$ on day 300. It thereafter decreases at a rapid rate to a value of 5×10^7 $L_{\odot}$ by day 900. On the other hand, the infrared (IR) light curve exhibits a slow increase from 4×10^8 to 8×10^8 $L_{\odot}$ between days 20 and 300, followed by a more rapid increase to $\sim 1.5 \times 10^9$ $L_{\odot}$ by day ∼500 (Fransson et al. 2014; Gall et al. 2014; Jencson et al. 2016).

A decline in UVO luminosity combined with a rise in IR indicates the presence of dust in the environment which absorbs and reprocesses the UVO photons to IR. The presence of dust is also supported by the gradual blueshifting of the intermediate-velocity emission lines of hydrogen and oxygen (Smith et al. 2012; Gall et al. 2014). Moreover, the gradual increase in blue–red asymmetry over time suggests that the receding part of the ejecta is increasingly being blocked by the presence of new dust which is lying interior to the line-emitting shocked gas (Smith et al. 2008).

[1] CRESST II/CUA/GSFC.
[2] CRESST II/UMBC/GSFC.

The origin of IR emission in Type IIn SN can be attributed to (a) an echo from the preexisting dust (Bode & Evans 1980; Dwek 1983; Andrews et al. 2011a), (b) emission from the newly formed dust in the postshock cool dense shell (Pozzo et al. 2004; Smith et al. 2008; Chugai 2009; Gall et al. 2014), (c) emission from dust formed in the SN ejecta (Kotak et al. 2005; Andrews et al. 2011b; Szalai & Vinkó 2013), or a combination of these.

The preexisting dust, which has survived the shock breakout, resides outside the vaporization radius of the explosion (Draine & Salpeter 1979). The luminosity of the shock–CSM interaction front is generally much lower than the instantaneous flash of energy at the time of outburst (Dwek & Arendt 2008; Soderberg et al. 2008). Therefore, the temperature of the surviving dust grains emitting in the form of an IR echo should be much smaller than the vaporization temperature of the grains. However, analysis of the IR excess indicates the dust temperatures to be close to vaporization temperatures at early epochs (Fransson et al. 2014).

Given the high dust temperature and the asymmetric extinction of the red and blue wings of the emission lines, Gall et al. (2014) rule out IR echo as a possible scenario in this case. Andrews et al. (2011a) argue in favor of IR echo. However, the shock breakout luminosity assumed in their study is much lower compared to the one estimated by theoretical models (Blinnikov et al. 2000) or from IR observations (Dwek & Arendt 2008).

The CCSN ejecta is a well-known site for dust synthesis. However, due to the presence of radioactive elements (such as ^{56}Ni, ^{56}Co, and ^{44}Ti), γ-rays, and energetic Compton electrons (Cherchneff & Dwek 2009; Sarangi & Cherchneff 2013), the earliest epoch of dust synthesis in the ejecta is not before day 250. Therefore, the dense shell that formed in the postshock CSM has been considered as the most potent source of dust causing the near-IR excess at day 60 onwards (Gall et al. 2014). Nevertheless, dust formation in such environments is controlled by a complex chain of processes, such as the cooling rate of the shocked gas, radiative heating by the forward shock, the reverse/reflected shock traversing inwards to the ejecta, and the radioactive processes of the inner ejecta expanding into the CSM.

The detection of a near-IR excess as early as day 60, as in the case of SN 2010jl, poses new challenges to our understanding of the dust formation scenario in any circumstellar environment. The dynamics of such high-density postshock gas, controlled by strong ionizing radiation and rapid cooling, have never been studied before. We formulate a model to address the following issues:

1. What is the earliest epoch of new dust formation in the CSM? Can the IR echo from the preexisting dust contribute to the light curve?
2. What are the physical and chemical processes that facilitate or impede the synthesis of dust in postshock gas?
3. What are the primary heating sources of the dust, present at various regions of the stellar system, that give rise to the IR emission?

This paper is arranged in the following order. In Section 2, we study the X-ray, UVO, and the IR signatures of the SN 2010jl light curve and their manifestation on the physical model. Following that, in Section 3, we present a schematic diagram of a typical Type IIn SN in light of its pre- and postexplosion morphology. Thereafter, additionally, we also focus on the probable dust compositions that can be derived from the observations. Following that, we address scenarios in all of the possible regions where preexisting dust can survive or new dust can form, in Section 4. Since dust formation in the postshock gas is the main focus of this paper, Section 5 deals with the constraints imposed on the preexplosion CSM and the postexplosion shock dynamics of SN 2010jl. In Section 6, we discuss the evolution of the postshock gas leading to conditions favorable for forming dust. Following that, in Section 7, we briefly summarize the physical and chemical processes that aid the formation and growth of dust grains in such environments. Lastly, in Section 8, we describe the energetics of the environment and the role played by the newly formed dust grains in explaining the IR emission in SN 2010jl. We summarize our results on SN 2010jl in Section 9 and their global implications for any Type IIn SN.

2. The Optical and NIR Fluxes

In this section, we analyze the UVO and IR observations of SN 2010jl and their implications on its light curve.

The optical and NIR observations of SN 2010jl at several epochs have been obtained using different facilities such as the *HST*, the 2.5 m Nordic Optical Telescope, the KeplerCam instrument at the F. L. Whipple Observatory in Arizona, and the *Spitzer Space Telescope* (Andrews et al. 2011b; Fox et al. 2011, 2013; Fransson et al. 2014).

Using the tabulated magnitudes provided by Fransson et al. (2014), we have calculated the fluxes in the optical bands u', B, V, r', and i' through the Vega flux zero-point conversions. The NIR fluxes for the J, H, and K_s bands were calculated using the Two Micron All Sky Survey standard system. The tabulated optical and NIR fluxes were interpolated on a uniform grid between the earliest and latest epochs of observations.

Within the timescale of UVO observations, the *Spitzer* 3.6 and 4.5 μm fluxes of SN 2010jl are available at days 87, 254, 465, 621, and 844 (Andrews et al. 2011b; Fox et al. 2013; Fransson et al. 2014). We fit the SED continuum at these five epochs. The fluxes at the r' band are likely to be dominated by the Hα line intensities (Fransson et al. 2014); therefore, we chose to ignore this band for the purposes of continuum fitting.

The spectra were fit using a two-component fit model with a blackbody as the UVO component and any of these: (a) a blackbody, (b) optically thin astronomical silicate dust, or (c) optically thin pure amorphous carbon as the IR component (Figure 1). For IR regimes of the electromagnetic spectrum, the wavelengths are much larger compared to the average grain radii ($\lambda_{\rm IR} \gg a$). Within this Rayleigh limit, the derived dust masses are independent of the grain sizes. For simplicity, a single grain of radius 0.01 μm and a single temperature were assumed.

The optical constants for the dust grains are derived from Weingartner & Draine (2001) and Zubko et al. (2004), respectively, for silicates and carbon dust. The best-fit scenarios for all 15 cases (5 epochs, 3 cases) are shown in Figure 1. The parameters obtained by the best-fit cases are summarized in Table 1.

The IR fluxes of SN 2010jl for late times (days 993, 998, 1368, and 1750) were obtained from the *Spitzer* Heritage Archive[3] database. There are no UVO and near-IR fluxes recorded for those epochs. We fit the two *Spitzer* points at each

[3] http://irsa.ipac.caltech.edu/applications/Spitzer/SHA/

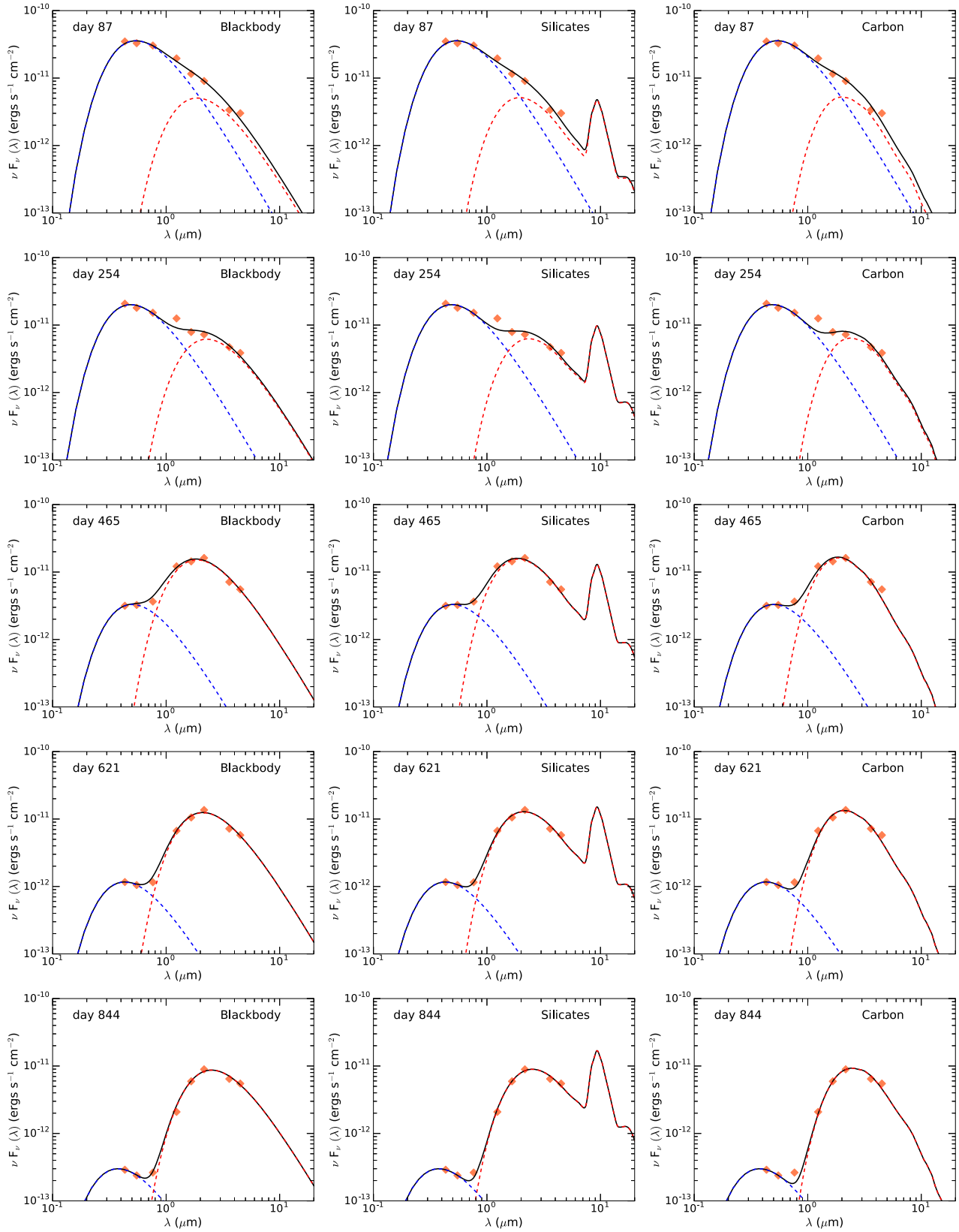

Figure 1. Fluxes in the optical (B, V, i') and the NIR (J, H, K_s) bands of SN 2010jl along with those in the *Spitzer* 3.6 and 4.5 μm bands at days 87, 254, 465, 621, and 844 (Andrews et al. 2011b; Fox et al. 2013; Fransson et al. 2014) are shown in the figure. The fluxes are fitted using a two-component fit with a blackbody fitting the UVO component (in blue) and any of these: (a) a pure blackbody, (b) astronomical silicate (Weingartner & Draine 2001), or (c) amorphous carbon dust (Zubko et al. 2004) fitting the IR component (in red). The error bars on the data points are too small to be visible on the figures. The best-fit scenarios obtained from the study are presented in Table 1.

Table 1
Best-fit Parameters to the Photometric Data of SN 2010jl

Epoch (days)	T_{UVO} (K)	R_{UVO} (cm)	L_{UVO} ($L_\odot$)	IR Component	T_{IR} (K)	R_{IR} (cm)	L_{IR} ($L_\odot$)	Dust Mass ($M_\odot$)
				BB	1959	1.4×10^{16}	5.1×10^{8}	⋯
87	6787	3.0×10^{15}	3.6×10^{9}	Sil	1566	⋯		1.8×10^{-3}
				Am-C	1368	⋯		4.4×10^{-4}
				BB	1613	2.2×10^{16}	6.3×10^{8}	⋯
254	7518	1.9×10^{15}	2.1×10^{9}	Sil	1322	⋯	⋯	4.9×10^{-3}
				Am-C	1159	⋯	⋯	1.3×10^{-3}
				BB	1971	2.3×10^{16}	1.5×10^{9}	⋯
465	7311	8.0×10^{14}	3.4×10^{8}	Sil	1613	⋯	⋯	4.7×10^{-3}
				Am-C	1486	⋯	⋯	8.8×10^{-4}
				BB	1735	2.7×10^{16}	1.2×10^{9}	⋯
621	8545	3.5×10^{14}	1.2×10^{8}	Sil	1445	⋯	⋯	6.5×10^{-3}
				Am-C	1313	⋯	⋯	1.4×10^{-3}
				BB	1460	3.2×10^{16}	8.8×10^{8}	⋯
844	9742	1.4×10^{14}	3.0×10^{7}	Sil	1238	⋯	⋯	9.5×10^{-3}
				Am-C	1126	⋯	⋯	2.2×10^{-3}
993	⋯	⋯	⋯	BB	1063	5.8×10^{16}	7.9×10^{8}	⋯
998	⋯	⋯	⋯	BB	995	5.6×10^{16}	5.8×10^{8}	⋯
1368	⋯	⋯	⋯	BB	855	6.3×10^{16}	3.9×10^{8}	⋯
1750	⋯	⋯	⋯	BB	709	7.6×10^{16}	2.7×10^{8}	⋯

of these late epochs using a pure blackbody and estimate the temperature, blackbody radius, and luminosity of the IR emission. The best-fit scenarios are shown in Figure 2 and listed in Table 1.

The UVO component of the spectra represents the emission from the shocked cooling gas, also referred to as the photosphere. The effective temperature of this region is found to be between 6000 and 8000 K. The photospheric luminosity is found to decline with the passage of postexplosion time. This is likely to be caused by a systematic decline in CSM density toward the outer radii, a decline in shock velocity over time, or a combination of both.

The blackbody radius (R_{UVO}) of the UVO component, derived from the fit, represents the minimum radius of the photosphere. The R_{UVO} is found to recede as a function of time, as shown in Figure 3 (top right) and in Table 1. By contrast, the prime source of the UVO emission is understood to be the shocked gas coupled to the outwards moving shock front, and hence R_{sh} (the position of the shock) should be increasing with time. This ambiguity is caused essentially by the shell becoming increasingly thin to optical radiation. In other words, the dense shell acts like a diluted blackbody with a dilution coefficient f_d ($=R_{sh}/R_{UVO}$), which is increasing as a function of time.

We also calculate the UVO luminosity in uniform temporal bins in order to reconstruct the UVO light curve. The evolution of L_{UVO} was thereafter fitted using a power law, $t^{-\beta}$, with $\beta = 0.55$ before day 310 and $\beta = 4.0$ thereafter. The best-fit scenario is presented in Figure 1 (top left). The nature of the luminosity, $L(t)$, derived in this study compares well with the findings by Fransson et al. (2014), Jencson et al. (2016), and Gall et al. (2014). The rapid decline in luminosity at later times can be attributed to a change in the density profile at the shock front. A similar drop in luminosity is also reflected in the evolution of the X-rays along the line of sight (Chandra et al. 2015).

2.1. Possible Source of the IR Emission

In this study, good fits to the IR spectra of SN 2010jl, shown in Figure 1, were achieved using the contribution from any of the three sources (a blackbody, astronomical silicates, amorphous carbon) as the IR component. Therefore, the best-fit models do not have any strong bias toward any of the three sources being the most likely one.

A blackbody fit is appropriate when the dusty shell is optically thick. Additionally, the blackbody radius (R_{IR}) represents the minimum possible radius of the dusty shell from where the IR emission originates.

The NIR fluxes can be fit well using the absorption coefficients of optically thin astronomical silicates. The upper limit on the 9.7 μm flux at late times was obtained from the *SOFIA* observations (Williams & Fox 2015). It indicates the absence of silicate features. Therefore, the presence of silicates is doubtful, unless the grains are large ($a \sim 5$ μm) or the dusty shell is optically thick.

With only photometric data in the 2.2–4.6 μm region, many featureless dust species can fit the spectrum. We choose carbon as a likely dust type owing to its relatively large abundance in space compared to other metals. Moreover, the studies dealing with the IR spectra from the preexplosion era also hint at the presence of carbon dust in SN 2010jl (Dwek et al. 2017). However, the CSM of SN 2010jl is reported to have a N-rich (Fransson et al. 2014) C-depleted environment ($N/C = 25 \pm 15$, $N/O = 0.85 \pm 0.15$). In such environments, O-rich dust species are known to be the primary dust components and all of the carbon mostly gets locked up in CO molecules (Sarangi & Cherchneff 2013). To support this argument, the observation of a N-rich dusty shell around massive stars, such as the Homunculus nebula surrounding Eta Carinae, does not show any evidence of C-rich dust species (Morris et al. 2017). Hence, the presence of amorphous carbon dust in SN 2010jl also becomes uncertain.

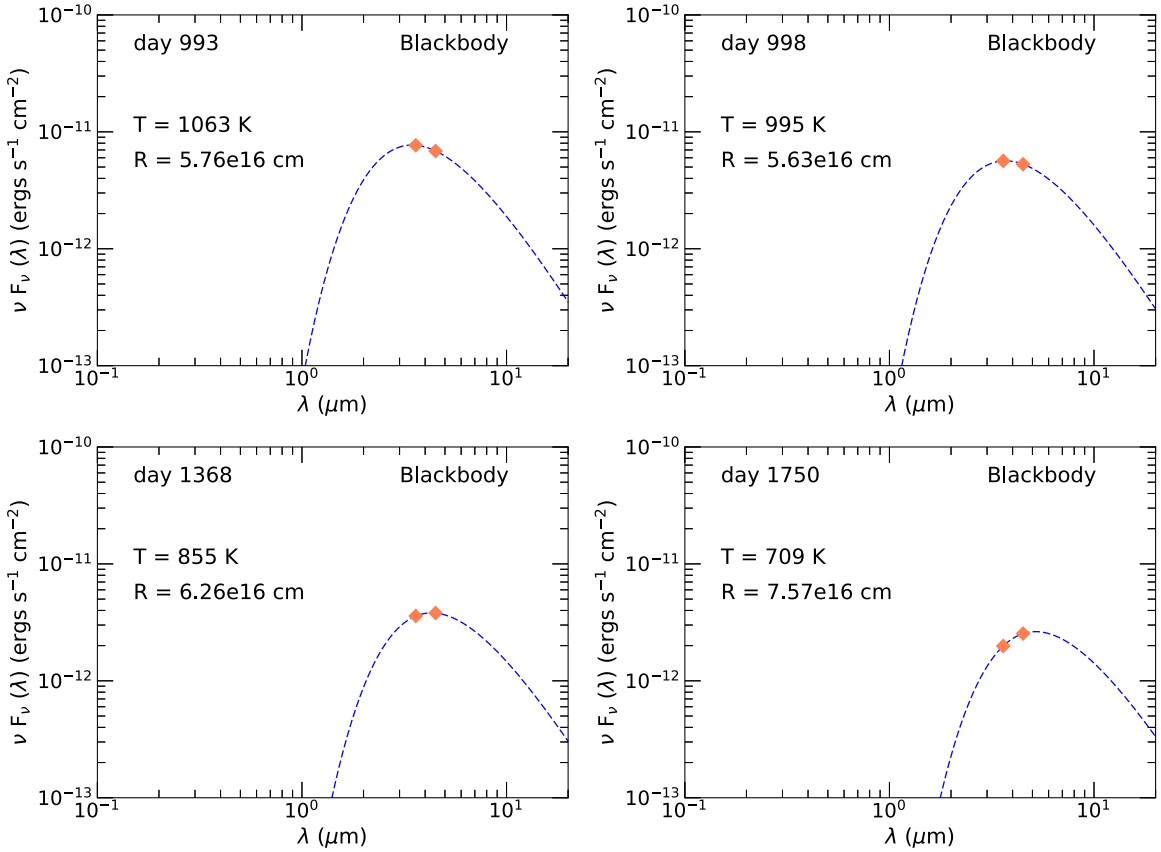

Figure 2. A pure blackbody is used to fit the *Spitzer* 3.6 and 4.5 μm data at late times (*Spitzer* IRSA) in order to derive the IR blackbody radius and the range of dust temperatures at late times.

Apart from identifying the types of dust, the best-fit scenarios also provide the boundary conditions to the shell morphology. Figure 3 presents the total IR luminosity, dust blackbody radii, temperatures, and masses as a function of time. The $L_{\rm IR}$ is found to increase steadily until day $\sim$500, followed by a slow decline phase. Importantly, around day $\sim$350, it is found to exceed the declining $L_{\rm UVO}$. The dust grains are found to remain at fairly high temperatures ($T > 1000$ K) at all times, providing additional constraints on the evolution of the shock radii. The dust masses grow steadily over time, with a small decrease between days 250 and 460 for both silicates and carbon dust. All the observed luminosities in the X-rays, UVO, and the IR are summarized in Figure 4 (Chandra et al. 2015; Fransson et al. 2014; Gall et al. 2014; Maeda et al. 2013).

3. Shell Morphology

Based on observational constraints, we formulate a schematic model of the preexplosion star and postexplosion SN, shown in Figure 5. For simplicity, we assume a spherically symmetric geometry.

Prior to the explosion, the progenitor of a typical Type IIn SN is composed of the central star, most likely in its supergiant phase, surrounded by a dense CSM (Chugai & Danziger 1994). The region between the stellar photosphere and the surrounding CSM is characterized by a low-density region, which might be extremely thin, making the CSM and the photosphere almost adjacent to one another, or it might also be a sizable fraction of the total CSM thickness (Dwarkadas 2007). The size of this region is determined by the mass-loss history of the central star, which may vary from being periodic to continuous in nature.

Following the explosion, the SN produces a blast wave that encounters the CSM within a few days. Thereafter, the forward shock traverses outwards through the CSM. Simultaneously, due to the ejecta–CSM interaction, a reverse/reflected shock that travels inwards through the ejecta is also generated. Owing to the high densities in the CSM, it is unclear whether the backward shock is a reverse shock or is reflected in nature. We consider it to be a reverse shock in the context of this study. The distinct regions in the shell–ejecta morphology along the radially outward direction are described as follows:

(a) the stellar remnant in the form of a neutron star or black hole,
(b) the expanding ejecta powered by the explosion energy,
(c) the reverse/reflected shock traveling inwards through the expanding ejecta,
(d) a thin layer of hot and ionized ejecta following the reverse shock,
(e) the cool dense shell formed by the cooling of the forward and the reverse shocks,
(f) a layer of adiabatically heated and compressed CSM immediately behind the forward shock,
(g) the forward-shock propagating outwards,
(h) the partially ionized CSM, ionized by the precursor radiation, lying ahead of the forward shock, and
(i) the region outside the evaporation radius where dust still survives.

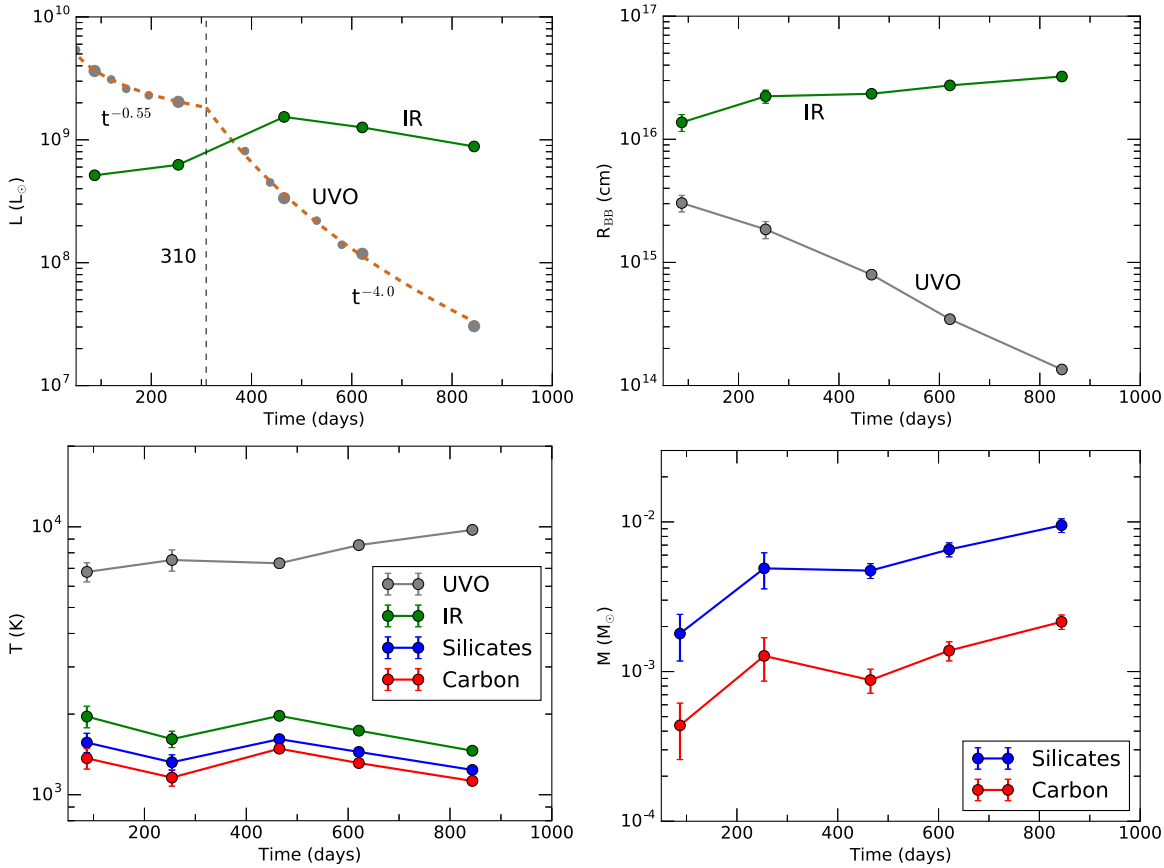

Figure 3. The postexplosion conditions, obtained by the fitting of the optical and IR bands, are presented in the figure: (a) the luminosity of the UVO component and the IR component, (b) the radius of the two blackbody components, (c) the temperatures of the optical as well as the three different IR components, and (d) the masses of astronomical silicates and amorphous carbon. The luminosity was obtained by interpolating and fitting the optical (B, V, i') and the NIR (J–H–K_s) fluxes from Fransson et al. (2014) at several epochs, in addition to the five epochs (days 87, 254, 465, 621, 844) for which we have *Spitzer* data. Thereafter, the luminosity, $L(t)$, was fitted using a power law of time. The exponents are found to be −0.55 and −4.0 with a switch at day ~310, as shown in the figure.

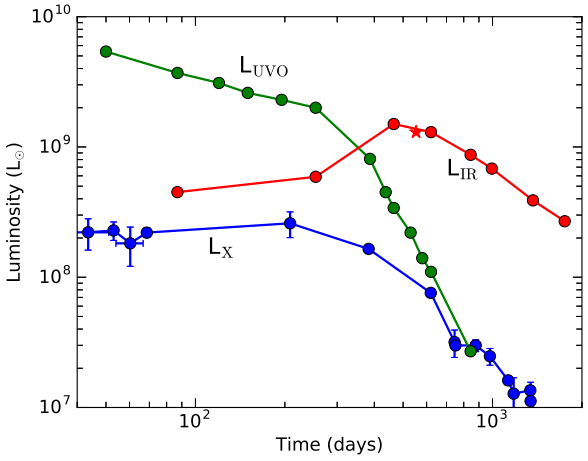

Figure 4. The luminosity of the observed UVO, X-rays, and IR as a function of time is presented, as obtained from the studies by Chandra et al. (2015), Fransson et al. (2014), Gall et al. (2014), and Maeda et al. (2013; marked by an "asterisk"). The IR luminosity at day 995 is an average of the IR luminosities at days 993 and 998.

The ejecta and the CSM are taken to be separated by the contact discontinuity throughout the span of the evolution.

The SN forward shock is capable of heating and ionizing the CSM that produces a strong flux of ionizing radiation. Owing

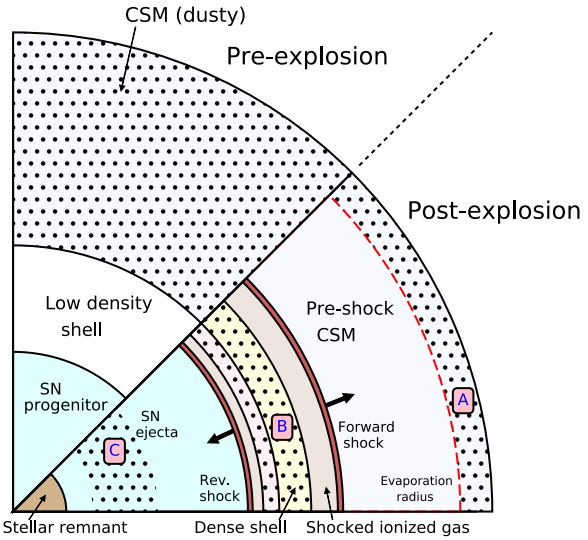

Figure 5. The schematic diagram presents the preexplosion stellar environment and the postexplosion ejecta–shell geometry of a typical Type IIn SN. The possible regions where dust can reside, marked in the figure with dotted meshes, are the following: (A) the preexisting dust outside the evaporation radius, (B) newly synthesized dust grains in the dense shell formed in the postshock cooling gas, and (C) new dust formed in the SN ejecta. Therefore, if IR emission is recorded in the postexplosion era, it should originate from any of these regions.

to the high densities, the postshock gas forms a thin dense layer of rapidly cooling gas which emits efficiently in the UVO regimes of the electromagnetic spectra. The total luminosity from this thin layer of hot postshock gas overall dominates the SN light curve. The total luminosity of the ejecta, powered by the radioactive decay of ^{56}Ni, ^{56}Co, and ^{44}Ti, is much smaller than that generated by the shock–CSM interaction (Gall et al. 2014; Jencson et al. 2016). Therefore, the energetics of the shock–CSM interaction determines the photosphere of the SN light curve (Fransson et al. 2014).

4. Origin of the Dust Emission

Figure 5 indicates the possible regions where dust can reside in the stellar system postexplosion. The IR emission can be due to the contribution from the (i) newly formed dust in the expanding ejecta, (ii) preexisting dust in the unshocked CSM, (iii) newly formed dust in the cooling postshock gas, or a combination of these. In this section, we shall briefly discuss cases (i) and (ii) in order to explain why new dust formation in the ejecta or the surviving dust in the preshock CSM cannot entirely account for the IR emission in SN 2010jl.

4.1. Dust in the Ejecta

The SN ejecta is not expected to be the main source of dust responsible for the IR emission in SN 2010jl because of the following reasons:

(a) Newly formed dust in the ejecta is not likely to contribute to the observed IR emission during either the early or late epoch of the evolution of the light curve. Theoretically, dust formation is impeded by the presence of radioactivities and the cascade of hard radiation and nonthermal electrons in the ejecta. This picture is observationally confirmed in the most extensive studies of SN1987A, where dust formation commenced only after day 250 of the explosion (Bouchet & Danziger 1993; Wooden et al. 1993; Dwek & Arendt 2015). By contrast, the IR excess from the SN commenced on day 30 after peak emission (Fransson et al. 2014; Gall et al. 2014).
(b) The blackbody radius of the IR-emitting region is 1.5×10^{15} cm, so even if dust somehow formed early on in the metal-rich ejecta, the dust could not have traversed this distance within 30 days at the typical ejecta velocity of 3000 km s^{-1}.
(c) Ejecta dust could in principle contribute to that late-time (>300 days) IR emission. However, this dust would be internal to both the forward and the reverse shock. The UVO will therefore never be attenuated by the dust, and its emission will consequently have to be always larger than that of the NIR emission, contrary to observations.

Taking into account all these factors, the ejecta of Type IIn SNe are likely to be a rather inefficient dust producer, so the majority of IR emission must be originating from the CSM.

4.2. The Preexisting Dust in the CSM

Pre-SN imaging of the field around SN 2010jl has provided upper limits on the UVO and NIR emission from the SN (Dwek et al. 2017; Fox et al. 2017). These upper limits suggest the need for the presence of preexisting dust in the CSM to extinguish the UVO emission from any hot progenitor star. Such dust will reprocess the emission produced by the shock breakout and by the ensuing SN shock traveling through the CSM, giving rise to an IR echo. The intensity and duration of the echo depend on the amount of preexisting dust and on the radius of the cavity within which the dust was vaporized by the breakout luminosity. A full discussion and a detailed model of the echo contribution to the SN light curve will be presented in a separate publication (E. Dwek et al. 2018, in preparation).

However, the echo will not contribute much to the late-time ($t > 300$ days) IR emission. The rise in the IR light curve around day 300 will require a delay time of 150 days, which corresponds to a dust-shell radius of 4×10^{17} cm. As shown in E. Dwek et al. (2018, in preparation), the mass of dust required to produce such an echo exceeds the abundance of refractory elements likely to reside in the CSM at that distance. Also, the dust temperatures at such a large distance do not comply with the range of temperatures derived from observations.

The ejecta dust or the preexisting dust is therefore inadequate to account for the IR luminosities in SN 2010jl. Newly formed dust in the CSM is therefore the dominant source of the IR emission at times later than day 300. In the following section, we present a detailed analysis of the formation of dust in the CSM.

5. The Postshock Gas Dynamics

The formation of dust grains in the shocked cooling gas requires appropriate gas-phase conditions. In order to resolve the postshock gas dynamics, in this section we focus on the constraints on the model, which are derived from the studies of the pre-SN CSM and the evolving SN shock.

5.1. CSM Dynamics

The evolution of the shock through the CSM is addressed analytically by several studies (Chevalier 1982; Chugai 2009; Ofek et al. 2010, 2014b). In the case of SN 2010jl, we adopt a power law for the evolution of the shock velocity, $v(t) \sim v_0 (t/t_0)^k$, and derive the values of k from the evolution of the hydrogen column densities. The preshock CSM density is considered to vary as $n \sim r^{-w}$ (Chevalier 1982; Svirski et al. 2012).

The UVO and X-ray luminosities of SN 2010jl are characterized by a broken power law with a break around day 310 ($=t_b$), as explained in Figure 3 (top left; Fransson et al. 2014; Jencson et al. 2016). The different exponents of the light curve before and after day 310 are attributed to the variation in the density index w.

The shock velocity ($v_{\rm sh}$), the radius at the shock front ($R_{\rm sh}$), and the column density and mass of the shocked gas, $N_{\rm H}$ and M, respectively, are derived as follows:

$$\begin{aligned} v_{\rm sh}(t) &= v_0\left(\frac{t}{t_0}\right)^{k_1}, \qquad t \leqslant t_b \\ &= v_b\left(\frac{t}{t_b}\right)^{k_2}, \qquad t > t_b \\ v_b &= v_0\left(\frac{t_b}{t_0}\right)^{k_1}, \end{aligned} \tag{1}$$

$$R_{\rm sh}(t) = R_0 + \int_{t_0}^{t} v_0\left(\frac{t}{t_0}\right)^{k_1} dt, \qquad t \leqslant t_b$$
$$= R_b + \int_{t_b}^{t} v_b\left(\frac{t}{t_b}\right)^{k_2} dt, \qquad t > t_b$$
$$R_b = R_0 + \int_{t_0}^{t_b} v_0\left(\frac{t_b}{t_0}\right)^{k_1} dt, \tag{2}$$

$$n(r) = n_0\left(\frac{r}{R_0}\right)^{-w_1}, \qquad R_{\rm sh} \leqslant R_b$$
$$= n_b\left(\frac{r}{R_b}\right)^{-w_2}, \qquad R_{\rm sh} > R_b$$
$$n_b = n_0\left(\frac{R_b}{R_0}\right)^{-w_1}, \tag{3}$$

$$N_{\rm H}(R_{\rm sh}) = \int_{R_0}^{R_{\rm sh}} n_0\left(\frac{r}{R_0}\right)^{-w_1} dr, \qquad t \leqslant t_b$$
$$= N_{\rm H}(R_b) + \int_{R_0}^{R_{\rm sh}} n_b\left(\frac{r}{R_b}\right)^{-w_2} dr, \qquad t > t_b, \tag{4}$$

$$N_{\rm H}({\rm tot}) = N_{\rm H}(R_{\rm l})$$
$$N_{\rm H}({\rm LOS}) = N_{\rm H}(R_{\rm l}) - N_{\rm H}(R_{\rm sh}), \tag{5}$$

$$M(R_{\rm sh}) = \int_{R_0}^{R_{\rm sh}} 4\pi r^2 \rho_0\left(\frac{r}{R_0}\right)^{-w_1} dr, \qquad t \leqslant t_b$$
$$= M(R_b) + \int_{R_0}^{R_{\rm sh}} 4\pi r^2 \rho_b\left(\frac{r}{R_b}\right)^{-w_2} dr, \qquad t > t_b, \tag{6}$$

where v_0, t_0, n_0, ρ_0 and v_b, t_b, n_b, ρ_b are the shock velocity, time, CSM number, and mass density at R_0 and at the break (R_b) on day 310. $N_{\rm H}$(LOS) represents the H column density along the line of sight. Using Equations (2) and (4), we can derive the time dependence of the column densities, which is an observable quantity:

$$R(t) = R_i + \frac{v_i t_i}{k_1 + 1}\left[\left(\frac{t}{t_i}\right)^{k_1+1} - 1\right]$$
$$\frac{dN_{\rm H}}{dt} = v(t) \times \frac{dN_{\rm H}}{dr}$$
$$= n_i v_i\left(\frac{t}{t_i}\right)^{k_1}\left(1 + \frac{v_i t_i}{(k_1+1)R_i}\left[\left(\frac{t}{t_i}\right)^{k_1+1} - 1\right]\right)^{-w_1}, \tag{7}$$

where $i = 0$ and b before and after the break, respectively.

5.2. Constraints from Observations

Chandra et al. (2015) and Ofek et al. (2014a) studied the X-ray emission data from SN 2010jl using the *Chandra*, *NuSTAR*, and *Swift X-ray* telescopes. The hydrogen column densities in front of the shock along the line of sight, which provide the necessary limiting conditions on the shock parameters at a given epoch, is derived by Chandra et al. (2015). The total H column density of the pre-SN CSM is estimated to be $\sim$1–2 $\times$ 10^{24} cm^{-2}.

The radial density dependence in the first phase, before the break in the density law, was assumed to be $w_1 = 2$, which resembles a freely expanding outflow. The lower limit on R_0 is the photospheric blackbody radius $R_{\rm UVO}$.

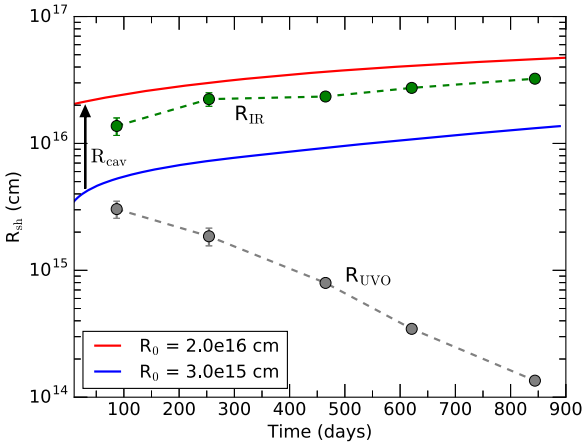

Figure 6. The evolution of the shock radius as a function of postexplosion days is presented for two sets of R_0. The shock radius ($R_{\rm sh}$) is compared to the evolution of $R_{\rm UVO}$ and $R_{\rm IR}$ in the figure. Assuming dust forms in the postshock region, the shock radius should be at least at $R_{\rm IR}$ as that is the minimum radius of the dusty shell. In order to satisfy this condition, the R_0 is chosen to be at least 2.0 $\times$ 10^{16} cm, and a low-density shell of thickness $R_{\rm cav}$ accounts for the gap between the ejecta and inner radius of the CSM.

The X-ray observations provide the gas column densities along the line of sight, i.e., the preshock CSM at a given time. We fit the hydrogen column densities from SN 2010jl using the above equations to determine the initial conditions such as m, w, R_0, n_0, v_0, etc. It is important to note that there is no unique solution to the column density function, as it depends on the appropriate combination of all these parameters. In Figure 6, the temporal variation of the shock radius is shown for two sets of inner radii, $R_0 = 3 \times 10^{15}$ cm, which is the lower limit of R_0 given by $R_{\rm UVO}$, and $R_0 = 2 \times 10^{16}$ cm.

Despite being a good fit to the observed column densities, the model with $R_0 = 3 \times 10^{15}$ cm cannot appropriately justify the SN light curve of SN 201jl. This is because the shock radius in this case is always less than the blackbody radius of dust ($R_{\rm sh} < R_{\rm IR}$), as clearly seen in Figure 6.

The preexisting dust has already been ruled out to be the only source of IR emission, and the X-ray observations put constraints on the maximum shock velocities. Hence, starting at $R_0 = 3 \times 10^{15}$ cm, the shock radius at a given time will never exceed the IR blackbody radius. On the other hand, emission from the postshock dust requires $R_{\rm sh} > R_{\rm IR}$, which is satisfied by models with $R_0 \geqslant 1.4 \times 10^{16}$ cm, which is the minimum blackbody radius of the IR emission.

We choose an inner radius of $R_0 = 2 \times 10^{16}$ cm, which provides a good fit to the observed column densities and also ensures that the condition $R_{\rm sh}(t) > R_{\rm IR}(t)$ remains valid all throughout.

A typical red supergiant has a photospheric temperature between 2500 and 3000 K and a luminosity of about 10^6 $L_\odot$. Therefore, the preexplosion star is assumed to have a photospheric radius between 10^{14} and 10^{15} cm. If the inner radius of the CSM (R_0) is larger than 10^{16} cm, there must have been a low-density region lying between the stellar photosphere and the surrounding CSM before the explosion. The possible existence of low-density cavities between the progenitor star and its CSM is not unexpected. Such cavities can be created by episodal mass-loss events and strong stellar winds (Castor et al. 1975; Dwarkadas 2007; Smith 2016).

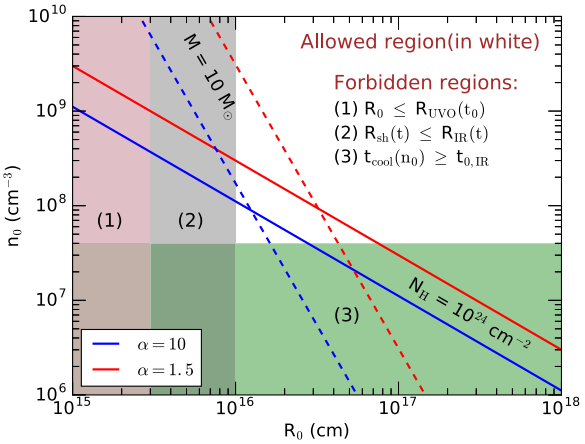

Figure 7. The figure shows the boundary conditions on the parameter space, in terms of n_0 and R_0. The solid lines correspond to the column density of 10^{24} cm^{-2} whereas the dotted lines correspond to the total CSM of 10 $M_\odot$ for two sets of the R_1/R_0 ratio (α = 1.5, 10). The white region in the figure is the allowed regions, whereas the shaded regions are forbidden due to various factors as noted in the figure. (See Section 5.)

To derive further constraints, in Figure 7 we present the the total column density ($\sim$1–2 $\times$ 10^{24} cm^{-2}) and the total mass of the CSM ($\sim$10 $M_\odot$) in the parameter space of n_0 and R_0. The n_0–R_0 relation is shown for two different R_1, given by α (=R_1/R_0) and taken to be 1.5 and 10. This diagram helps all possible combinations of n_0 and R_0 that comply with the X-ray, UVO, and IR observations to be identified.

The choices of n_0 and R_0 were constrained by the following requirements:

1. The inner radius of the CSM (R_0) must be equal to or larger than the observed blackbody radius of the photosphere, R_{UVO}.
2. The shock radius ($R_{sh}(t)$) must be larger than the blackbody radius of the IR spectra ($R_{IR}(t)$) so that the dust formation region is internal to the propagating shock front.
3. The shortest cooling time ($t_{cool}(n_0)$) of a parcel of shocked gas should be smaller than the earliest epoch of dust formation ($t_{0,IR}$). This is because the shocked gas is required to cool down below condensation temperatures before the onset of dust formation.

Based on these allowed ranges of n_0 and R_0, the best-fit model for the observed column densities (N_H) has been constructed. Table 2 summarizes the initial conditions for the model and the temporal variations of the physical quantities such as density, shock velocity, and shock radius.

The fit to the hydrogen column densities along the line of sight is shown in Figure 8 (top left) with the swept-up column in the postshock gas. The number density in the CSM prior to the explosion is presented in Figure 8 (bottom right). The evolution of the pre- and postshock CSM mass (top right) and the velocity of the forward shock (bottom left) through the dense CSM is also shown in the figure. The total mass of CSM in this case is about 12 $M_\odot$, which aligns well with the studies by Smith et al. (2012) and Fox et al. (2017). The shock velocity steadily declines with time exponents of -0.25 and -0.5 before and after the break at day 310.

6. Cooling of the Postshock Gas

In this section, we study the temporal evolution of the shocked gas and determine the suitable conditions that facilitate dust formation in SN 2010jl.

Various studies have analytically or numerically addressed the shock equations relevant to a parcel of gas, assuming either equilibrium or nonequilibrium conditions (Draine & McKee 1993; Truelove & McKee 1999; Dessart et al. 2015). In this case, we adopt a similar formalism to solve the energy, momentum, and continuity equations simultaneously and to derive the time-dependent temperature, density, and velocity profiles in the postshock shell.

The passage of a shock with velocity of $\sim$4000 km s^{-1} through a parcel of gas heats it to temperatures of $\sim 10^8$ K. Thereafter, the gas behind the shock cools very rapidly, initially by free–free and X-ray line emission, and then through atomic-line cooling, down to temperatures of $\sim 10^4$ K. The appropriate cooling functions relevant to this study are defined by Dalgarno & McCray (1972), shown in Figure 9. At temperatures higher than 10^4 K, the gas is fully ionized and the cooling function reaches its maximum between 10^5 and 10^6 K. Below 10^4 K the cooling depends on the residual ionization of the gas (see Figure 9), which is mainly controlled by metals such as Fe, Si, and Mg. Cooling from H^+, H, and molecular lines are also dominant in such low temperatures. For this regime, we chose an ionization fraction of 10^{-4}, which corresponds to a lower cooling rate (Dalgarno & McCray 1972), in our calculations. The shaded region in Figure 9 represents a zone that is characterized by a very low cooling rate and low ionization fractions, both of which induce the formation of a warm dense shell which has minimal further cooling. The rate of cooling per unit volume of the gas is given by $\eta(T) = n_e n_H \Lambda(T)$.

To study the evolution of the postshock gas, the momentum and energy equations (Cox 1972; Cox & Raymond 1985) are solved with respect to a parcel of gas that has been shocked by the SN blast wave. The postshock jump conditions for mass density (ρ), pressure (p), shock velocity (v_s), and gas temperature (T) are given by $\rho_J = 4\rho_0$, $p_J = 3/4\ \rho_0 v_s^2$, $v_J = 1/4\ v_s$ (in the frame of the shock), and $T_J = 1.47 \times 10^{-9}\ v_s^2$, where v_s is in cm s^{-1}. The density and temperature in the postshock gas evolve as

$$\frac{d\rho}{dt} = \frac{\rho\eta(T)}{\rho_0 v_s^2}\left(\frac{5}{2} - 4\frac{\rho_0}{\rho}\right)^{-1}, \tag{8}$$

$$\frac{T}{T_0} = (1 + M^2)\frac{\rho_0}{\rho} - M^2\frac{\rho_0^2}{\rho^2}, \quad M^2 = \frac{\rho_0 v_s^2}{p_0}$$

$$= M^2\frac{\rho_0}{\rho}\left(1 - \frac{\rho_0}{\rho}\right) \quad (\text{for, } M_1 \gg 1), \tag{9}$$

where M is the Mach number of the medium. By integrating Equation (8) and simultaneously using the ρ–T relation from Equation (9), the density and temperature of a parcel of gas in the postshock CSM are determined.

In Equation (9), as T/T_0 is always positive, ρ is always greater than ρ_0. In order to maintain continuity with the jump conditions, we have $\rho \geqslant 4\rho_0$. Therefore, the number density continues to increase over time, and the drop in temperature is governed by the cooling curve (Figure 9).

Equations (8) and (9) do not include any heating of the shocked gas by the downstream radiation from the shocked

Table 2
The Number Density, Shock Velocity, and Shock Radius at t_0 and t_b Estimated from the Best Fit to the Postexplosion Column Densities

Parameter	Value at t_0 ($w_1 = 2$)	Variation	Value at t_b ($w_2 = 4.76$)	Variation
CSM density	$n_0 = 1.45 \times 10^8$ cm^{-3}	$\sim r^{-2}$	$n_b = 5.7 \times 10^7$ cm^{-3}	$\sim r^{-4.76}$
Shock velocity	$v_0 = 5.5 \times 10^8$ cm s^{-1}	$\sim t^{-0.25}$	$v_b = 3.8 \times 10^8$ cm s^{-1}	$\sim t^{-0.5}$
Shock radius	$R_0 = 2.0 \times 10^{16}$ cm	$\sim t^{0.75}$	$R_b = 3.2 \times 10^{16}$ cm	$\sim t^{0.5}$

gas. In the case of such a high-density medium, the shocked gas tends to cool rapidly within a period of a few days. The shock front, which is spatially close to the cooling gas, generates a strong flux of ionizing X-rays and UVO radiation. This radiation flows downstream and acts as a continuous heating source to the postshock gas. When the gas temperature is high ($>10^4$ K), the gas is already fully ionized and so the impact of the downstream ionizing radiation is minimal. However, at temperatures below 10^4 K, hydrogen starts to become partially neutral, forming traces of H_2 molecules in the gas. Currently, there are no accurate tools available that can handle the hydrodynamics and radiative transfer through such a high-density semi-ionized gas to study all of the relevant cooling mechanisms. We therefore calculated the postshock temperatures using the following postprocessing procedure.

The densities are sufficiently high ($>10^{12}$ cm^{-3}) in the postshock cooling gas, and the environment is expected to reach steady state reasonably fast. On that basis, a steady-state radiation transfer model is a fair and acceptable approximation. Therefore, we use the spectral synthesis code CLOUDY (Ferland et al. 1998) to study the radiation transport through the postshock gas at temperatures lower than 10^4 K. Even though CLOUDY is a static code, several snapshot cases were modeled in order to account for the time evolution of the postshock gas.

The luminosity in the UVO, X-ray, and IR bands, generated by the forward shock, is shown in Figure 4. The UVO emission is generally found to be about one order of magnitude higher than the total X-ray luminosity (Chandra et al. 2015), and both decline steadily after day 310. Since the line intensities do not play any role in our calculations, we approximated the X-ray flux by a 10^8 K free–free bremsstrahlung spectrum. Similarly, the UVO spectra can also be presented as a blackbody with the appropriate temperature, as shown by Fransson et al. (2014) and Gall et al. (2014). Using this simplification, the spectra of the initial SED were constructed as an input to code CLOUDY, presented in Figure 10.

Analytically, the energy-loss term in Equation (8) is replaced with $H(T) = \eta(T) - S(T)$, where $S(T)$ is the additional heating in units of erg cm^{-3} s^{-1} accounting for the downstream radiation from the shock front. Owing to the presence of the continuous heating source, the dn/dt term decreases significantly, and hence n tends to remain almost unaltered at low temperatures when $\eta(T)$ becomes comparable to $S(T)$.

The observed UVO spectra at all epochs peak around $\sim 0.3\,\mu$m which corresponds to a temperature of around 8000 K as also confirmed by Fransson et al. (2014) and Gall et al. (2014) and shown in Figure 10. Therefore, most of the radiation in the optical band comprises non-ionizing photons with energies lower than 13.6 eV. On the other hand, even though the luminosity of the X-rays is lower, the ionizing soft X-ray photons between wavelengths 10^{-3} and $0.1\,\mu$m contribute significantly to the heating of the gas. Figure 10 (left panel) shows the spectra that are generated by the CSM–shock interaction and the spectra of the downstream radiation after passage through the column of dust-free gas. The shaded region (in blue) in the figure represents the total radiation that is absorbed by the gas per unit time. So, the remainder of the downstream radiation is responsible for heating the dust grains when they are formed.

Figure 10 (right panel) shows the temperatures of the postshock gas as a function of column density, under the circumstances when (a) the downstream radiation is ignored, (b) only the heating by the X-rays are considered, and (c) only the heating by the UVO radiation is considered. When the downstream radiation is not taken into account, it is evident that the gas cools rapidly in the absence of any heating source. However, in reality, due to the heating by the downstream radiation, the postshock gas remains warm for a prolonged period.

As shown in Figure 10 (right panel), at early times, day $\sim$200, the entire column of postshock gas remains hotter than the condensation temperatures, which is around 2000 K. Therefore, the formation of dust grains is unlikely in these regimes. After day 375, the luminosity of the shocked gas decreases rapidly, and the postshock gas is able to cool below 2000 K, marking the onset of dust formation. The heating of the gas is initially dominated by the UVO emission and by the X-ray heating at later times. The rate of energy absorption by the gas due to heating by X-rays and UVO is compared in Figure 17.

The complete temperature and density profiles of the postshock gas are shown in Figure 11. At a given epoch, the gas is fully ionized and temperatures are higher than 10^6 K up to a column density of a few times of 10^{22} cm^{-2} behind the SN shock. Following that, the rest of the column in the postshock gas is at much lower temperatures, as shown in Figure 11 (left panel). The gas density in the postshock gas, shown in Figure 11 (right panel), increases gradually from 10^8 cm^{-3} with a steep rise at the column density of $\sim 10^{23}$ cm^{-2} to reach a density between 10^{13} and 10^{14} cm^{-3} following the n–T relation (Figure 11).

Therefore, the postshock gas dynamics lead to the formation of a reservoir of warm and dense gas in the postshock shell, with nearly steady temperatures ranging between 1000 and 3000 K. The shaded region on the cooling function in Figure 9 depicts the temperature zone of the warm dense shell where the heating and cooling rates tend to balance each other. Importantly, this is the region of interest for dust formation.

Calculations show that the gas temperature decreases with the amount of column density traversed by the radiation field. We define $N_{\rm min}$ as the minimum column density the radiation must traverse before the gas temperature drops down to 2000 K. $N_{\rm min}$ is proportional to the luminosity of the source. Therefore, as the luminosity of the SN shock decreases with time, $N_{\rm min}$ also simultaneously decreases.

$N_{\rm min}$ was calculated using CLOUDY by studying the radiation transport through the postshock gas at various epochs. Figure 12 compares $N_{\rm min}$ to the postshock column density $N_{\rm H}(R_{\rm sh})$ as a function of time. Importantly, the boundary

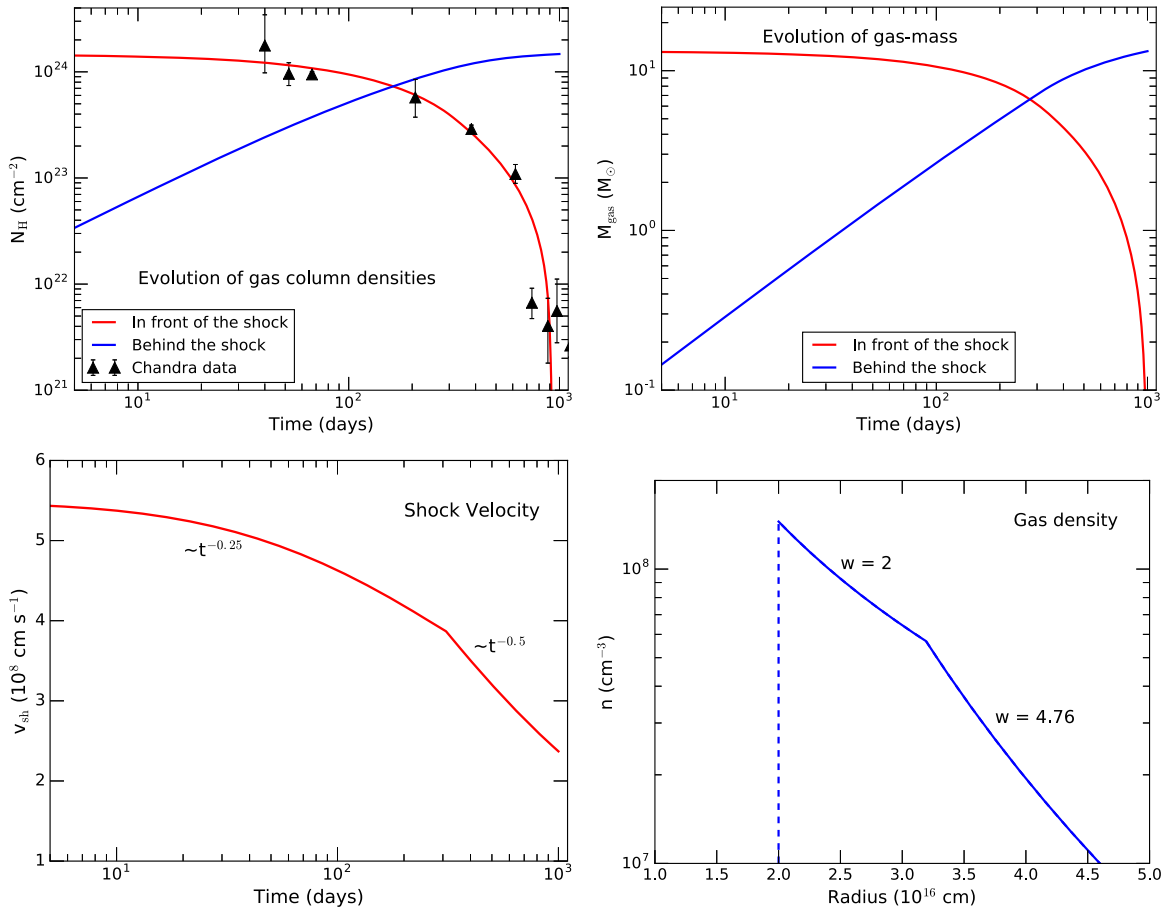

Figure 8. The preshock CSM and the evolution of the postshock gas are characterized by the following parameters, with reference to Table 2: (a) the evolution of the hydrogen column density, calculated using Equations (2) and (4), (b) the evolution of the CSM mass behind and ahead of the shock front, (c) the evolution of the shock velocity, and (d) the CSM density profile as a function of radius, before the encounter with the shock.

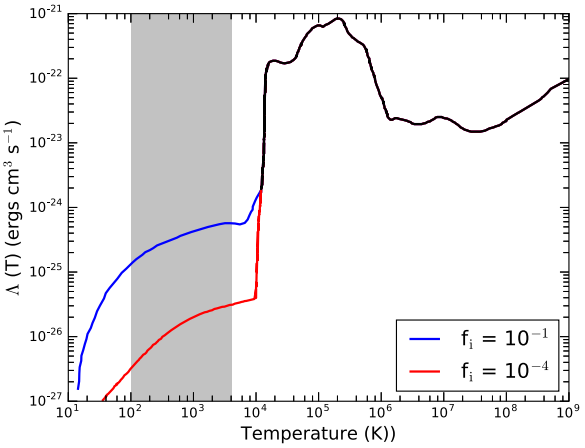

Figure 9. The cooling functions, $\Lambda(T)$, for two different ionization fractions ($f_i = 10^{-1}$, 10^{-4}) at low temperatures is shown in the figure, which is taken from Dalgarno & McCray (1972). For temperatures larger than $\sim 10^4$ K, the entire gas is fully ionized. The shaded region in gray represents the zone of interest, in terms of dust formation.

condition for dust formation in the postshock shell is therefore defined by $N_{\rm H}(R_{\rm sh}) > N_{\rm min}$, which occurs around day 380, as shown in the figure. The dashed line in Figure 12 represents the amount of gas in the column density, which is below the condensation temperature at a given time.

Figure 13 presents the total mass of the postshock gas and the mass of the gas that is below the condensation temperatures. As evident from the figure, from day 380 onwards, a fraction of the postshock gas becomes cold cold enough to sustain the formation of stable molecules and dust grains. Assuming the solar abundance of elements in the CSM, there are sufficient atomic species that can account for the mass of silicates that is comparable to the inferred silicate mass from observations. However, owing to the carbon-poor nature of the CSM (Fransson et al. 2014), there is not enough condensable atomic carbon that can account for the inferred carbon dust masses. This brings forward the possibility that the total dust mass can be constituted of the fraction of both silicates and carbon.

A shell of warm gas is known to cool adiabatically as it expands freely. However, in this case, adiabatic cooling and expansion have minimal impact on the evolution of the postshock gas because of the following: (a) the presence of a continuous source of energy at close proximity and (b) the large initial radius and very small thickness of the dense shell (ΔR) make $\Delta R/R$ small at all times ($\sim 10^{-6}$ at day 400). So, we can safely ignore the further expansion of the postshock shell due to adiabatic effects within the timescales of a few hundred days.

7. Conditions for Dust Formation

In this section, we shall discuss if and how dust can form and grow chemically in such environments when the suitable gas-phase conditions prevail.

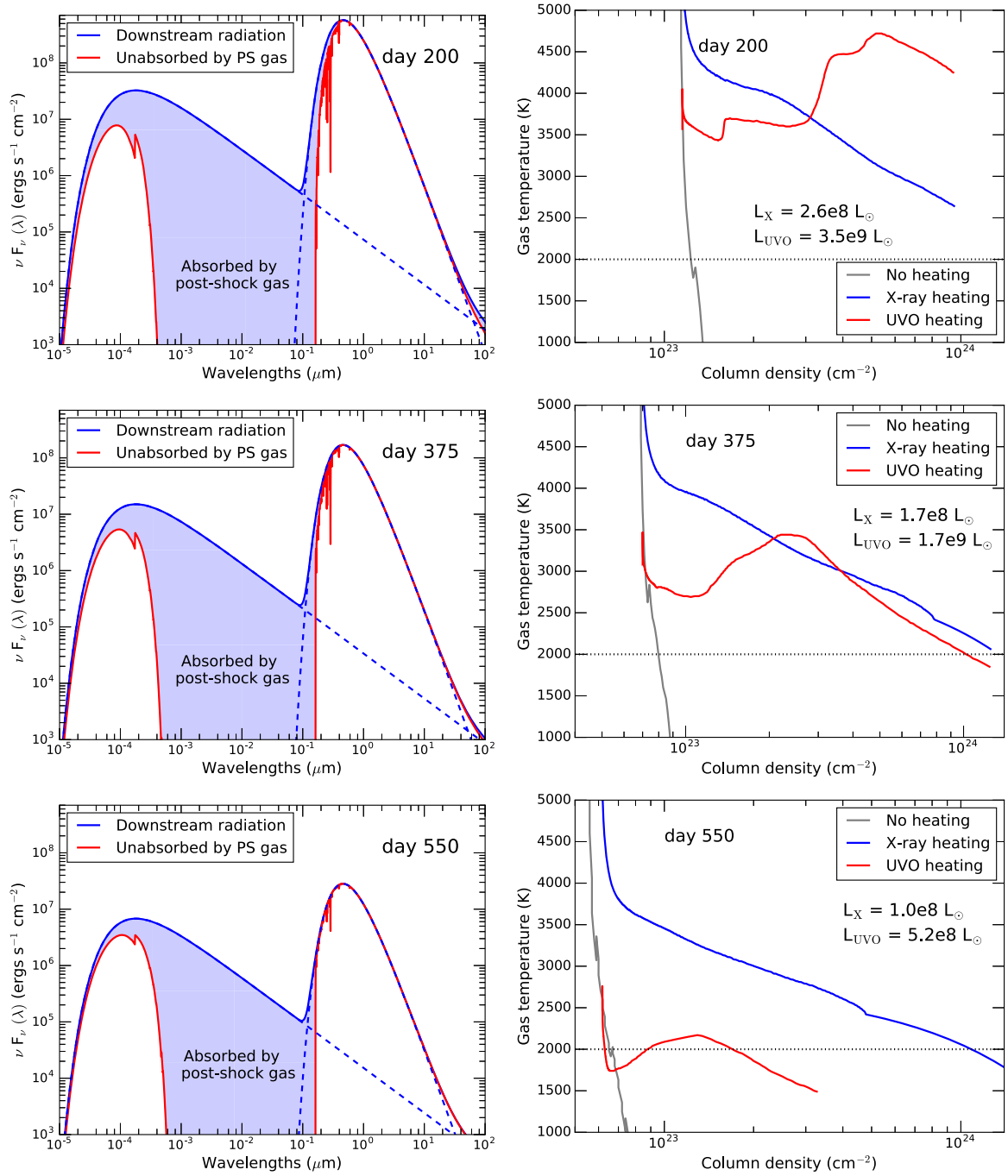

Figure 10. The figures in the left panel represent the spectra of the downstream radiation in terms of luminosity per unit shock area for three postexplosion epochs (days 200, 375, and 550). The flux of the downstream radiation, $F_\nu(\lambda)$, is calculated as $F = F_{\rm obs}(D^2/R_{\rm sh}^2)$, where $F_{\rm obs}$ is the observed flux and D is the distance of the supernova from the earth. The total downstream radiation (solid blue line), generated at the shock front, consists of the X-ray and the UVO component, shown by the blue dashed lines. The spectra of the unabsorbed radiation (in red), derived using the code CLOUDY, are the result of the attenuation and absorption by the column of dense dust-free postshock gas. The radiation absorbed by the column ($N_{\rm H}$) of postshock gas at a given time is shown by the shaded regions in the figures. The right panel shows the resultant gas temperature, at the same epochs, assuming (a) no downstream radiation, (b) downstream radiation from an X-ray source, and (c) downstream radiation from a UV–optical source. At early times, the gas temperature is found to be controlled by the bolometric luminosity. Later, the bolometric luminosity declines fast, and the gas temperature is mainly controlled by the residual X-rays.

The formation of cosmic dust in such dynamic environments is a kinetic process that is controlled by simultaneous phases of nucleation and condensation (Sarangi & Cherchneff 2013). The gas-phase nucleation leads to the formation of molecules and small clusters, whereas the stable gas-phase clusters grow in size through coagulation and accretion (Sarangi & Cherchneff 2015). Both phases require moderately high gas temperatures and high gas densities. The warm dense shell formed in the postshock gas provides ideal conditions that are conducive to dust and molecule formation after day ∼380, when the average gas temperature of the shell cools down below 2000 K and the gas densities are higher than 10^{13} cm^{-3}.

At high temperatures, the strong flux of ionizing photons and free electrons has destructive effects on any stable molecule formed in the medium. Molecule formation in the gas phase can transpire at around 3000 K when the ionization fraction is

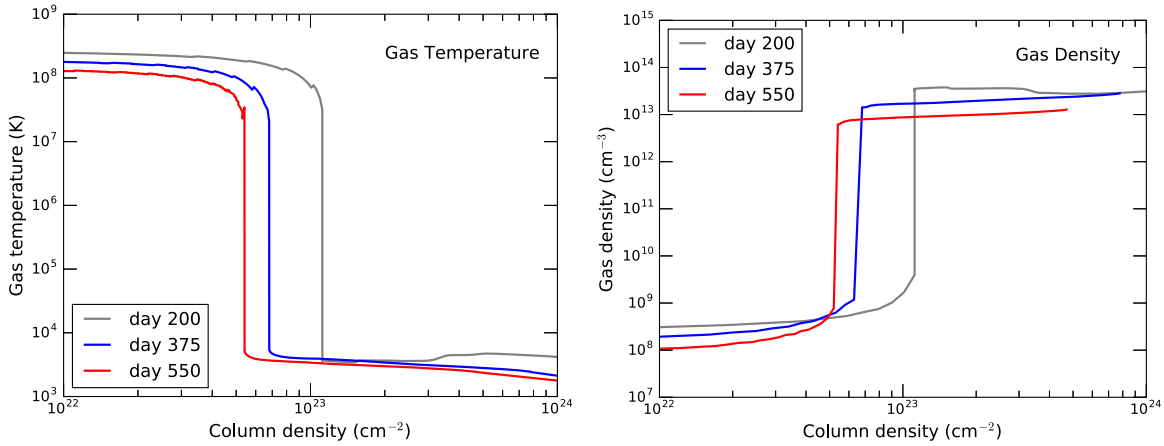

Figure 11. The postshock conditions of the CSM are presented in the following panels: (a) the profile of gas temperature as a function of postshock column density for three different epochs, and (b) the gas density profile of the postshock gas at three epochs. The temperature and density profiles are calculated taking into account the cooling of the shocked gas and the impact of the downstream radiation (X-rays and UVO) as a heating source.

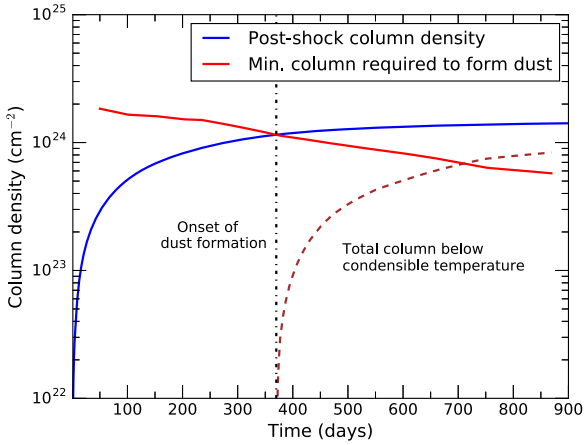

Figure 12. The minimum column density needed to be traversed by the shock, $N_{\rm min}$ (in red), before the gas temperature drops below the condensation temperature is plotted vs. time. Also shown is $N_{\rm H}(R_s)$, the total postshock column density vs. time (in blue). Dust can form in the postshock gas when $N_{\rm H}(R_s) > N_{\rm min}$.

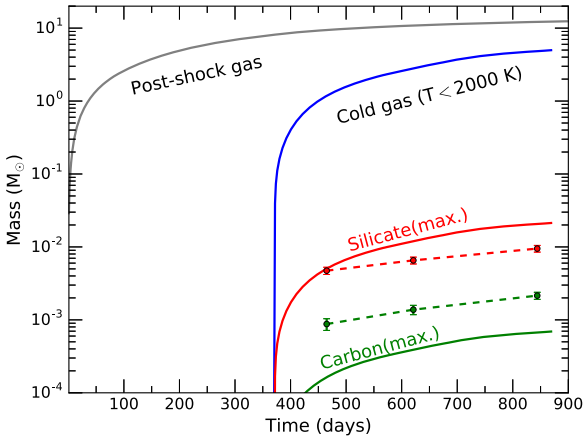

Figure 13. The figure shows the total mass of the postshock gas as a function of time. Also shown is the total mass of condensable elements at temperatures $T < 2000$ K. From the total mass of condensable metals present in the gas, the extreme upper limits on the silicate and carbon dust masses have been derived. Also, the inferred masses of silicate and carbon, obtained from fitting the IR data, are also shown in the figure with the dashed lines. The CNO abundance ratios are taken from Fransson et al. (2014).

Table 3
The Timescales for Different Chemical Processes that Transpire Simultaneously to Form a 0.01 μm Dust Grain

Process	Product	Timescale (s)[a]
Nucleation	$MgFeSiO_4$	0.13
Nucleation	C_n	17
Accretion	0.01 μm grain	380
Coagulation	0.01 μm grain	10^5

Note.
[a] Physical conditions in the text.

relatively low. However, newly formed dust grains with a temperature above 2000 K are most likely to sublimate instantaneously. In the context of this study, we do not implement a detailed chemical kinetic scheme to study the gas-phase chemistry. Instead, an empirical approach mainly focusing on the physical conditions that favor or impede dust formation in such environments and their manifestations on the SN light curve was adopted.

Table 3 lists the timescales for important chemical processes that lead to the nucleation and condensation of silicates and carbon dust.

A series of chemical reactions involving Si, O, H, Mg, and Fe leads to the formation of the seed molecular clusters that eventually condense to form astronomical silicates, as described by Goumans & Bromley (2012) and Sarangi & Cherchneff (2013). Similarly, the synthesis of amorphous carbon dust proceeds through the gas-phase nucleation of C chains and rings (Clayton et al. 1999; Cherchneff 2010; Sarangi & Cherchneff 2015). The rate of nucleation presented in Table 3 corresponds to the slowest process in the series of reactions within the first order of approximation. The temperature and densities used are the ones derived in the model, shown in Figure 11.

The timescale for accretion (Dwek & Cherchneff 2011) on a dust particle is given by

$$\tau_{\rm ac} \sim \frac{2 \times 10^{18}}{\alpha_S(T, T_d)}\, \rho_d \left(\frac{a_d}{\mu{\rm m}}\right)\left(\frac{n_{\rm H_2}}{\rm cm^{-3}}\right)^{-1}\left(\frac{\rm T}{\rm K}\right)^{-0.5}, \qquad (10)$$

where ρ_d is the density of the accreting dust particle, a_d is the grain radius in microns, $n_{\rm H_2}$ is the gas density, and the $\alpha_{\rm S}$ is the sticking coefficient.

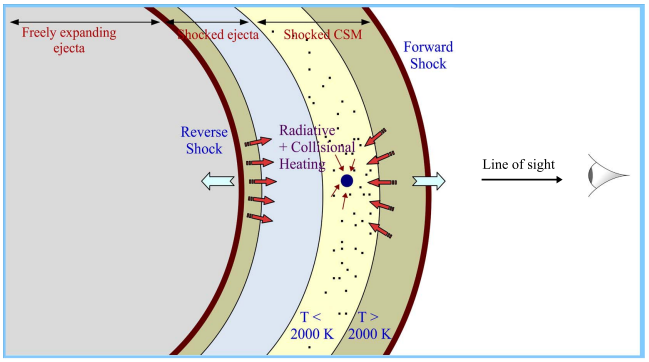

Figure 14. The cartoon presents the ejecta–CSM morphology at a given epoch when dust formation commences in the postshock shell. A hypothetical grain of dust is shown to be present in the dense shell defined by gas temperatures $T_g < 2000$ K. The dust grain is subjected to radiative heating by the forward and reverse shocks. Also, it is heated collisionally by the ambient gas. The arrows in red represent the radiation directed toward the dust grain. The forward shock moves toward larger radii, while the reverse shock moves inwards in the frame of the CSM.

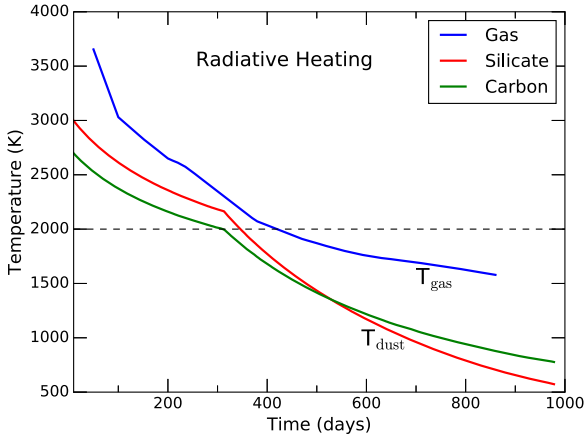

Figure 15. The figure presents the temperature of the gas and the dust in the postshock gas as a result of the heating by the downstream radiation only. The dotted line at $T = 2000$ K represents the condensation regimes. Hence, dust formation is infeasible before day 380 because the gas, heated by the X-ray and UVO, is not cold enough and also the radiation from the forward shock evaporates any dust grain that forms in the gas. The temperatures shown in the figure does not include the impact of collisional heat exchange between the gas and the dust.

The timescale to grow a 0.01 μm dust grain, assuming a number density of 10^{13} cm^{-3} and a sticking coefficient of 0.5 at 1000 K is ~380 s.

In the absence of available metals to accrete, the condensation process is dominated by the coagulation of small dust particles. In this density regime, where the mean free paths of particles are much greater than the grain radii, the coagulation between two particles (Jacobson 2005; Sarangi & Cherchneff 2015), say i and j, is dominated by Brownian diffusion with a rate given by

$$k_{i,j} \sim \pi(a_i + a_j)^2(\bar{v_i}^2 + \bar{v_j}^2)^{1/2}, \quad (11)$$

where v_i is the thermal velocity of particle i.

Assuming a dust-to-gas-mass ratio of $\sim 10^{-3}$ and the gas number density of $\sim 10^{13}$ cm^{-3}, the rate of coagulation between two 10 Å dust grains of silicate at 1000 K is $\sim 9.4 \times 10^{-3}$ cm^3 s^{-1}. In order to form a 0.01 μm grain, approximately one thousand 10 Å grains are required to coagulate. Hence, the timescale is $\sim 10^5$ s, which is a little over one day.

Therefore, given suitable conditions, the dust formation timescale in the postshock gas is only about one day. As suitable conditions prevail post-day 380, the postshock dense shell in SN 2010jl becomes a site of efficient dust synthesis.

8. Heating of the Dust Grains

The preceding sections have confirmed that dust formation in the postshock gas is feasible after ~380 days postexplosion and the newly formed dust has had sufficient time to grow in size. We shall now inspect all possible sources of heating the dust grains in order to account for the observed temperatures and IR luminosities.

Figure 14 is a schematic diagram that illustrates the heating sources of a hypothetical dust grain present in the dense shell behind the shock.

A dust grain is radiatively heated by the ionizing photons that are traveling downstream from the SN shock. Furthermore, the grain will also be heated by collision with the ambient warm gas in the dense shell. In addition, the dust grains are also subjected to heating by the reverse shock. Since the dusty shell is interior to the forward shock, the luminosity generated by the forward-shock–CSM interaction will not be obscured along the line of sight by the newly formed dust.

The downstream radiation from the forward shock gets gradually attenuated while passing through the postshock gas. The soft X-rays and UVO are entirely attenuated up to the Lyα continuum edge while passing through the column of postshock gas, as shown on Figure 10 (left panel). The optical radiation with a peak at 8000 K comprises mostly non-ionizing photons, which remain unabsorbed by the gas. They act as the primary heating source of the dust.

It is important to note that even though we can assume the incident spectra to resemble a blackbody, it is purely a mathematical substitution for the real physical picture. In reality, the gas around the forward shock that generates the downstream radiation is dilute (optically thin). The dilution coefficient is given by $f_d = R_{\rm sh}/R_{\rm UVO}$, as explained in Section 2.

8.1. Dust Temperatures

In this study, the temperature of a dust grain present inside the warm gas reservoir was calculated as a function of gas density, gas temperature, and the flux of downstream radiation. The collisional heating rate of a dust grain has been addressed by Dwek (1987) and Hollenbach & McKee (1979). At high densities, the gas and dust temperatures are coupled. When $T_d > T_{\rm g}$, collisions with the dust heat the gas and vice versa. Then, the heating/cooling rate of a dust grain by the gas is given as

$$\frac{dH}{dt} = n\bar{v}f_{\rm ed}\,\pi a^2(2kT_g - 2kT_d) \quad (12)$$

in terms of the gas density (n), mean thermal velocity ($\bar{v}$), geometric cross-section ($\sigma_d = \pi a^2$) of a dust grain, and the accommodation coefficient ($f_{\rm ed}$) of the fractional energy deposition (Hollenbach & McKee 1979).

The gas density in the shell varies between 10^{13} and 10^{14} cm^{-3}, whereas the average gas temperature of the reservoir gradually drops from 4000 K at early epochs to 1000 K over a couple of years.

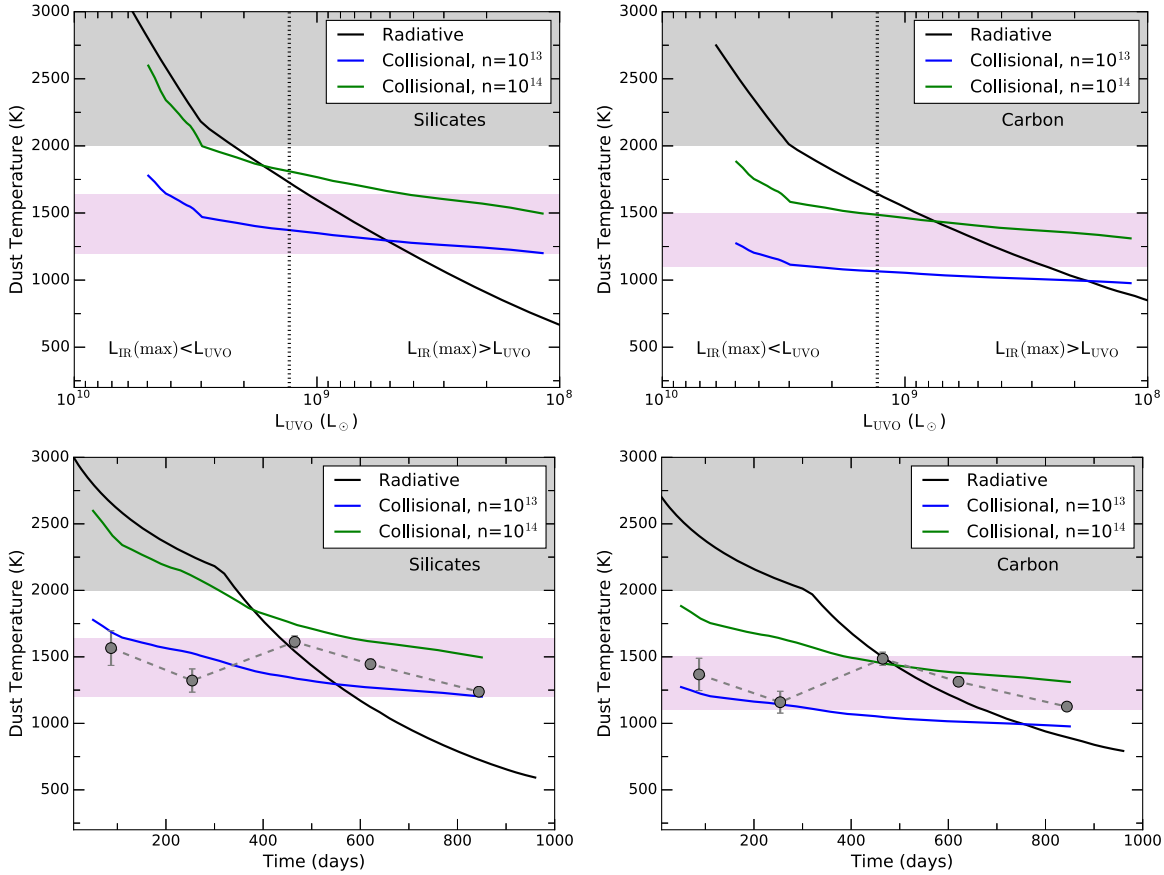

Figure 16. The figure shows the temperatures for an astronomical silicate (left panel) and an amorphous carbon (right panel) dust grain as a function of forward-shock luminosity and the corresponding postexplosion time. The impact of radiative and collisional heating on the dust temperature is calculated separately. The dust temperature at a give time t due to collisional heating by the gas at $T_g(t)$ is estimated for two gas densities, 10^{13} and 10^{14} cm^{-3}. The band marked in pink represents the observed dust temperature region, whereas the band in gray shows the region above the evaporation temperature. The top panel presents the dust temperatures as a function of the forward-shock bolometric luminosity, and the bottom panel presents the same as a function of postexplosion time in days. The best-fit dust temperatures to the observed IR spectra at various epochs are also shown in the bottom panel.

The first dust grains synthesized in the gas are a few angstroms in size. Such small grains, subjected to the general interstellar radiation field, are known to undergo temperature fluctuations. However, with a baseline temperature of ∼2000 K (gas temperature when the first grain condenses), the absorption of individual photons has a negligible effect on the temperature fluctuations. Furthermore, in spite of the high flux of photons, the cooling time is much shorter compared to the time between two photon absorptions. So, the impact of stochastic heating is negligible in this case.

The rate of radiative heating was calculated through the equilibrium heating and cooling balance (Dwek 1987) of the grains in the presence of the SN forward shock, where the source luminosity is $L_{\rm UVO}(t)$. Considering a 10 Å particle as a prototype of the smallest dust grain, the equilibrium temperatures were calculated for astronomical silicates and amorphous carbon dust. Figure 15 shows the dust temperatures for the two dust types when subjected to radiative heating by the SN shock. The gas temperature at the back end of the postshock shell (the region where the dust forms) is also presented as a function of time. The dashed line at 2000 K indicates the maximum temperature that can support the formation and survival of dust grains.

Due to the high luminosity of the forward shock, the equilibrium temperature of the fiducial grain is always higher than 2000 K for both dust types in the first ∼350 days. As the gas temperatures are also beyond condensation limits, there is no scope for dust formation or survival in this period.

Figure 16 illustrates the dependence of dust temperature on the ambient gas conditions. The higher the gas density, the more closely bound the dust temperature is to the gas temperature of the shell. It is evident from the figure that, for such high-density mediums like the warm dense shell, the dust temperature is heavily influenced by the collisional heating due to the surrounding gas. The band in pink marks the region of observed dust temperatures.

The final temperature of the grains is a combined effect of radiative and collisional heating and the energy exchange between the gas and dust. The figure shows that the dust temperatures fit well in the observed range of temperatures when the source luminosities are below $\sim 10^9\ L_\odot$ post-day 400.

The dotted vertical line in Figure 16 (top panel) represents the maximum IR luminosity, which corresponds to day ∼450. Furthermore, it divides the plot into two regions defined by $L_{\rm IR}({\rm max}) > L_{\rm UVO}$ and $L_{\rm IR}({\rm max}) < L_{\rm UVO}$. The dust temperatures in the region given by $L_{\rm IR} > L_{\rm UVO}$ complies with the observed band of temperatures. This supports the previous finding that dust formation in the postshock gas is possible when the luminosity of the forward shock is below $10^9\ L_\odot$ after day 350. However, since the dust is internal to the forward shock, the dust cannot obscure the UVO from the forward shock along the line of sight. Therefore, the UVO luminosity

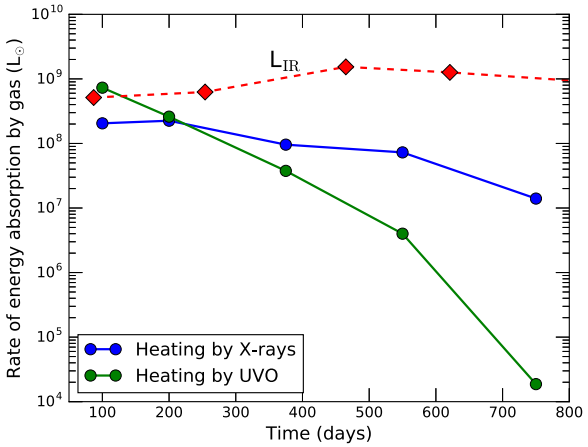

Figure 17. The rate of energy absorbed by the postshock gas, when heated by X-rays and UVO from the forward shock, is presented. Initially, the heating of the gas is dominated by the UVO, and later, the X-rays become more significant. Further, in the figure the energy absorption rate of the gas is compared to the observed IR luminosity from the dust. $L_{\rm IR}$ is found to be larger than the energy absorbed by the gas at a given time. Therefore, the exchange of heat between the gas and the dust cannot be the only source of energy that is heating the dust.

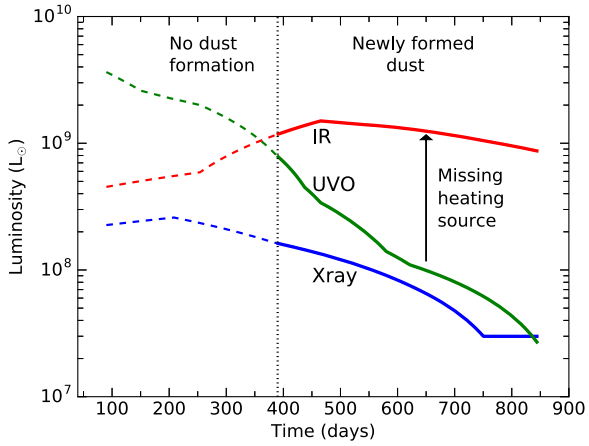

Figure 18. The observed luminosities from SN 2010jl are presented in light of its history of dust formation. The dotted lines before day 380 indicate the timescales where the IR emission is not from newly formed dust but is rather an IR echo. Later, when new dust forms in the postshock gas, the IR luminosity is always found to be larger than the X-ray and UVO luminosities from the forward shock. The arrow indicates the minimum luminosity of the reverse shock, which is the missing heating source, as it has no observational evidence. In all likelihood, the newly formed dust is thick to optical wavelengths and so it is efficiently scattering the incident radiation from the reverse shock that is interior to the dust-forming shell.

cannot be the primary heating source of the dust, because in that case the IR luminosity could not have exceeded the luminosity of the heating source.

The efficiency and time span of the collisional heating of a dust grain by the warm gas in the shell is limited by the total amount of energy that is stored at a given time in the heat reservoir. Post-day 300, the luminosity of the photosphere drops rapidly, hence the continuous supply of the energy to the heat sink also drops. At the same time, the IR luminosity increases steadily. So, the reservoir of warm gas would simultaneously start to cool down at a much faster pace as it loses energy via IR emission from the newly formed dust.

The total energy stored in the warm gas reservoir at a given instant is approximately $\sim 3/2\ NkT$. Assuming a 10^{24} cm^{-2} column of gas, with density 10^{13} cm^{-3} and temperature 1500 K, the total number of particles is given by 2×10^{58}, and the energy in the reservoir is therefore 4×10^{45} erg. At an IR luminosity of $10^9\ L_\odot$, the entire energy is radiated away in less than one day.

The rate of energy absorbed by the gas, heated by the radiation from the forward shock, is shown in Figure 17, along with the IR luminosity of the dust. The $R_{\rm IR}$ is found to be larger than the combined heating rate of the gas. Therefore, the transfer of energy from the gas to the dust due to collision cannot be responsible for the large IR luminosity at late times.

8.2. Constraints on the Reverse Shock

The UVO spectra from SN 2010jl correspond to the forward shock only. As the reverse shock is internal to the dust-forming region in the CSM, if the dust is optically thick, it can entirely conceal the UVO luminosity from the reverse shock. That energy is in that case absorbed by the dust grains in the CSM and reradiated at the IR wavelengths.

The observations in the UV, optical, or X-ray regimes do not provide any information about the properties of the reverse shock. So, it can be inferred that the entire reverse-shock spectrum has been reprocessed by the gas and dust present in the CSM.

Figure 18 presents the IR luminosity in the regime where new dust forms in the dense postshock gas. It is evident that at all times post-day 380, $R_{\rm IR} > (R_{\rm UVO} + R_{\rm X\text{-}ray})$. Therefore, the minimum luminosity of the reverse shock required, in order to provide the extra heating, is given by $R_{\rm rev}({\rm min}) = R_{\rm IR} - R_{\rm UVO} - R_{\rm X\text{-}ray}$.

The hard X-rays, having a low absorption cross-section, are unlikely to be absorbed by the 10^{24} cm^{-2} column of gas in the CSM. So, it provides an upper limit on the shock-induced gas temperatures as it should not produce any hard X-ray photons. The following points summarize the boundary conditions that can be inferred from this study.

1. The dust in the CSM must be thick to optical radiation.
2. The minimum $L_{\rm rev}$ is equal to $R_{\rm IR} - R_{\rm UVO} - R_{\rm X\text{-}ray}$ at a given time.
3. The reverse-shock velocity should be high enough such that the rate of mechanical energy generated is more than $L_{\rm rev}$.
4. The reverse-shock velocity should be low enough such that it does not produce hard X-rays by its interaction with the ejecta.

The IR luminosity reaches its maximum, which is $\sim 10^9\ L_\odot$, around day 500. In order to generate this luminosity, the rate of kinetic energy generated by the ejecta–reverse-shock interaction should be at least $10^9\ L_\odot$, which can then get transformed into heat. The minimum velocity ($v_{\rm rs}^{\rm min}$) of the reverse shock is defined by the relation

$$L_{\rm IR} = \frac{1}{2} \times \frac{dm}{dt} \times (v_{\rm rs}^{\rm min})^2 = 2\pi R^2 \rho (v_{\rm rs}^{\rm min})^3 . \qquad (13)$$

Taking the radius to be 2×10^{16} cm and the density at 500 days to be 10^{-13} g cm^{-3} (Nozawa et al. 2010; Sarangi & Cherchneff 2013), we obtain the minimum reverse-shock velocity required to be $\sim$250 km s^{-1}.

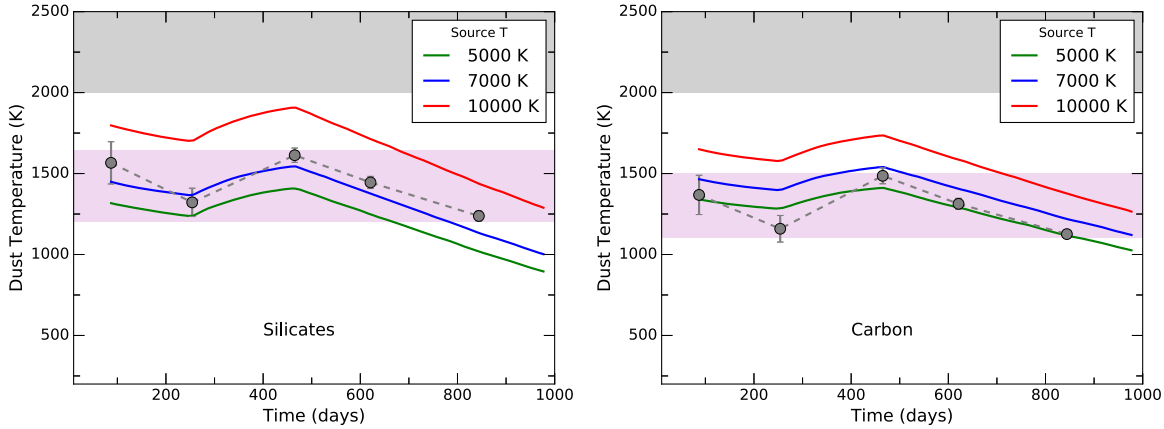

Figure 19. The figure presents the resultant temperatures for a silicate (left) and a carbon (right) dust grain of 0.01 μm radius as a function of postexplosion time for various source temperatures when they are heated by the reverse shock only, assuming $L_{\rm rev}(t) = L_{\rm IR}(t)$. The pink band represents the range of observed dust temperatures, while the gray band represents the region where the dust temperature is above the condensation temperature of the grains. The impact of collisional heating by the ambient gas is not shown in the figure. Additionally, as the dust is optically thick, the resultant temperature of the entire dusty shell cannot be determined by the equilibrium heating of a single dust grain only. See Section 8.2 for further explanations.

Hard X-rays above 3 keV (4×10^{-4} μm) have very low absorption cross-sections, as also evident from Figure 10. Taking $\lambda = 4 \times 10^{-4}$ μm as the highest energy, the maximum allowed jump temperature ($T_{\rm J} = hc/\lambda k$) of the shocked gas is 3.6×10^7 K. The maximum velocity of the reverse shock is therefore calculated from the relation

$$T_{\rm J} = \frac{3}{16}\frac{\mu_m}{k}(v_{\rm rs}^{\rm max})^2\,, \tag{14}$$

which is the jump condition and μ_m is the average mass of an atom. In O-rich SN ejecta, the mean molecular weight is around 17 (Sarangi & Cherchneff 2013). The maximum reverse-shock velocity is therefore given by $\sim$310 km s^{-1}.

For the sake of generality, we also consider a lower ejecta density of $\sim 1.7 \times 10^{-15}$ g cm^{-3} (Utrobin et al. 2017) and present an alternative set of parameters. In this case, the lower limit on the shock velocity, $v_{\rm rs}^{\rm min}$, calculated using Equation (13), increases to $\sim$950 km s^{-1}. Encounters with shocks of such velocity shock will lead to the production of some hard X-rays in the shocked ejecta. However, the shocked ejecta would be optically thick enough to cut off most of the hard X-rays. This explains the absence of hard X-rays in the spectra. The photo-attenuation cross-sections of O-rich gas at 3 keV, 10 keV, and 30 keV are 5.77×10^3, 1.58×10^2, and 10.1 barns, respectively (Veigele 1973). Assuming around 4 $M_\odot$ of O-rich gas in the shocked ejecta, the column density is about 10^{23} cm^{-2}, which is enough to ensure an optically thick medium.

As the dust is optically thick to the incident radiation from the inner heating source (reverse shock), we have limited information to characterize the incident spectra. Therefore, even though we have calculated the upper and lower limits on the shock velocity, luminosity, and dust masses, the temperature of the dusty shell cannot be determined accurately.

Figure 19 shows the temperatures of a hypothetical 0.01 μm grain of silicate and carbon when heated by the reverse shock, assuming the reverse-shock luminosity to be equal to the IR luminosity at a given time, which is basically the lower limit of the reverse-shock luminosity. Three different source temperatures were assumed, and the spectra was assumed to be a blackbody. The figure shows that the UVO radiation with a temperature ranging between 7000 and 5000 K fits well with the observed band of temperatures. Radiation in this range comprises of non-ionizing photons, hence it will not be able to ionize the gas efficiently. However, as shown in Figure 20, the dusty shell made up of 0.01 μm grains is not thick to radiation around 0.4–0.6 μm, which corresponds to a blackbody temperature in this range. So, a more likely scenario is provided by a source at higher temperature, which heats the gas and collisionally heats the dust. Additionally, as the dust is optically thick, it can shield the remainder of the gas from the strong flux of radiation generated by the reverse shock. Lastly, the dust is an efficient coolant, hence once the dust is formed in the dense shell, it further helps cool down the ambient gas.

8.3. Estimated Dust Masses

The total amount of dust at a given time depends on several intercorrelated physical and chemical processes, which we do not address in detail in the course of this current study. The constraints on the dust masses can be derived from the following: (a) the fit to the IR emission, (b) the maximum mass of metals that can condense, and (c) the minimum mass that can make the shell optically thick.

Table 4 presents the upper limit on the dust masses that can be synthesized in the postshock gas at a given epoch, purely from stoichiometric estimates. The upper limit of the silicate mass is larger than the observed masses, hence silicates can be a major dust component in the postshock shell. In the case of carbon dust, however, the maximum atomic carbon present in the gas is smaller than the mass that is required to fit the observations. Hence, carbon dust cannot be the only dust type present in the postshock gas.

However, the absence of silicate features at late times (Williams & Fox 2015) makes carbon a more likely dust species. This dichotomy can be resolved, if the dust comprises a combination of both silicates and carbon dust.

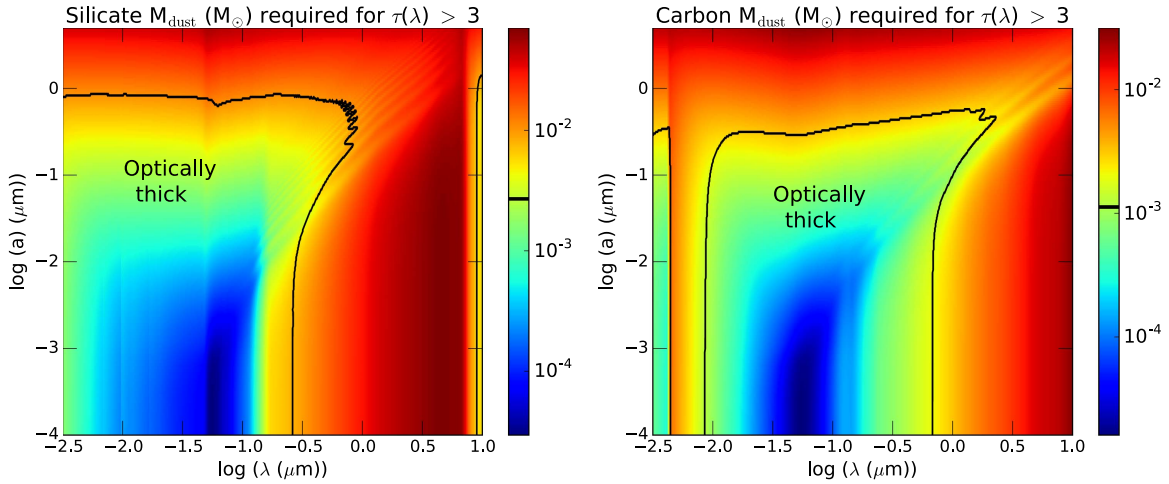

Figure 20. The required minimum dust mass to achieve $\tau(\lambda) > 3$ is shown as a function of wavelength and grain radius for silicates (left) and carbon (right) dust. The minimum optical depth $\tau(\lambda)$ that makes the dusty shell opaque to radiation at wavelength λ is taken to be 3. The colorbar for the mass (in $M_\odot$) is on the right side of each figure. The black contour indicates the enclosed regions where the required minimum dust mass is less than or equal to the observed mass of dust (6.5×10^{-3} $M_\odot$ for silicates and 1.5×10^{-3} $M_\odot$ for carbon). Therefore, the dusty shell is optically thick only if the grain radii and the wavelength of the incident radiation from the reverse shock are within the limits of the contour.

Table 4
Dust-shell Properties for Selected Days

Epoch (day)	Postshock Shell ($M_\odot$)	M_{sil} ($M_\odot$)			M_{car} ($M_\odot$)		
		Max.[a]	Observation	$\tau(U)$	Max.[a]	Observation	$\tau(U)$
465	8.2	3.5×10^{-2}	4.7×10^{-3}	1.7	1.1×10^{-3}	8.8×10^{-4}	3.7
621	9.9	4.2×10^{-2}	6.5×10^{-3}	2.4	1.3×10^{-3}	1.4×10^{-3}	5.8
844	11.7	5.0×10^{-2}	9.5×10^{-3}	3.5	1.6×10^{-3}	2.2×10^{-3}	3.1

Note.
[a] The maximum dust mass is purely a stoichiometric quantity, calculated using the solar mass fractions and the CNO abundances given by Fransson et al. (2014). It ignores the steps of formation of intermediate molecules during the process.

In a dusty shell like this one, where the inner radius is R_0 and the mass of dust is M_d, the optical depth is given by

$$\tau(\lambda) = \frac{M_d\ \kappa(a, \lambda)}{4\pi R_0^2}. \quad (15)$$

In Figure 20, we calculate the mass of dust (silicates and carbon) required in order to make the postshock shell thick to incident radiation. In terms of the optical depth (τ), $\tau_\lambda \geqslant 3$ is assumed as the necessary condition for optical thickness. The dust masses are shown in the grid of the grain radii and wavelength of incident radiation.

The contours of the dust masses (of silicates and carbon) that have been derived from observations are also presented in Figure 20. It is evident from the figure that the grains cannot be larger than 0.1 μm and also the incident spectra of the reverse shock should have a peak at wavelengths less than 0.3 μm. Therefore, the reverse-shock spectra cannot be dominated by the UVO only. It is also confirmed by the U-band optical depths listed in Table 4.

Importantly, this also confirms that the preexisting dust alone cannot account for the late-time IR emission. This is because the total mass of preexisting dust, which is present at radii larger than the evaporation radius, cannot be too large to make the region optically thick. That will lead to a violation of the maximum possible dust-to-gas-mass ratio.

On the other hand, the soft X-rays at wavelength λ, given by $\lambda < 0.1$ μm, are very efficient in heating and ionizing the gas. Strong ionizing radiation from the reverse shock is capable of collisionally destroying the dust grains that have formed in the postshock CSM. Hence, the allowed luminosity of the reverse shock should have the maxima of the spectral distribution between 0.1 and 0.3 μm.

9. Summary and Discussions

In this paper, we have studied the origin and evolution of the IR emission in SN 2010jl.

Our model has combined the results from the study of UVO and IR spectra by Fransson et al. (2014), Gall et al. (2014), Maeda et al. (2013), and Jencson et al. (2016), and the analysis of X-ray data by Chandra et al. (2015) and Ofek et al. (2014b). The morphology of the ejecta, adopted in this study, is consistent with hydrogen column densities estimated from X-ray analysis. The temperatures of the spectra representing the optical and the IR light curve, derived from the best-fit scenarios, are also akin to the estimates by Fransson et al. (2014).

The study confirms that the formation of new dust in the CSM or in the ejecta is not feasible as early as a few weeks after detection, as previously reported by Gall et al. (2014). Dust synthesis commences in the postshock CSM only after day 380 from the time of detection. Also, dust is unlikely to be present in the ejecta at the early times. So, the IR emission must be attributed to the circumstellar dust that has survived from the preexplosion era.

Eventually, at later times, the preexisting dust is gradually destroyed by SN shock encounter and then newly formed dust in the dense postshock shell acts as the prime source of IR emission. Therefore, the IR observations by *Spitzer* of SN 2010jl at days 465, 621, and 844 can be attributed to the new dust formed in the postshock shell. To explain the IR excess at day 87 and day 254, we shall address the case of IR echo from the preexisting dust in the associated paper (E. Dwek et al. 2018, in preparation).

Dust formation in the circumstellar shell of Type IIn SNe is controlled by radiative transfer processes. Downstream radiation from the shocked gas is responsible for directly heating the dust as well as passively heating the dust by ionizing the surrounding gas.

The presence of strong ionizing photons has a twofold impact on the chemical pathways: (a) it hinders the earliest epoch of dust formation, and (b) it also leads to the formation of the warm dense shell, so the gas-phase species get enough time to react via kinetic processes. Therefore, the high postshock density does not automatically ensure early dust formation, as previously estimated by Gall et al. (2014). In the absence of downstream radiation, the gas is likely to cool from 10^4 to $\sim$100 K in a span of less than a day, leaving very little time for the chemical reactions to proceed kinetically.

In this study, special emphasis has been given to the progenitor–CSM morphology in the preexplosion era. As the findings suggest, in order to explain the IR spectra of SN 2010jl, a low-density region, extending up to a few times 10^{16} cm and lying between the preexplosion star and the surrounding CSM, is absolutely necessary. In SNe, where a dense CSM almost superposes the progenitor star, the early formation of new dust becomes an unlikely scenario, both in the CSM and as well as in the ejecta. Therefore, in addition to the intensity of the radiation field, the shape of the outer CSM also determines the efficiency of dust formation.

In brief, the processes or phenomena that control the dynamics of dust formation in such environments can be summarized by the following points. The dust formation is facilitated by

1. the high density of the postshock gas,
2. the short cooling time,
3. the formation of the warm gas reservoir, which does not cool efficiently, and
4. a large inner radius of the CSM.

On the other hand, the formation and growth of dust in such an environment is impeded by

1. the X-rays and UVO from the forward shock,
2. the radiation from the reverse shock, and
3. collision with the ambient hot and ionized gas.

Even though Type IIn SNe have a relatively large progenitor in general, the final dust yield is influenced by strong circumstellar interactions. The CSM is constituted of materials ejected in the form of metal-depleted winds in the preexplosion era. Therefore, assuming the average mass of the CSM to be $\sim$10 $M_\odot$, an upper limit of about $\sim$0.1 $M_\odot$ of dust can be considered to form in the CSM. Hence, in the CSM, dust formation might transpire earlier than the ejecta, yet the final mass may not exceed 0.1 $M_\odot$. In the case of SN 2010jl, the dust mass ranges between 10^{-3} and 10^{-2} $M_\odot$.

This study has developed the first model that addresses the scenario of dust formation in circumstellar shells which are associated with strong ionizing radiation from the forward and reverse shocks of SNe. Even though the study is based on SN 2010jl, the effect of radiation on the postshock gas is globally applicable to any Type IIn SN to study dust formation in such environments.

There are some analytical steps in the model where some first-order approximations or simplifications were required. It is important to note that the effective cooling mechanism of a gas parcel that is at low temperatures ($T < 4000$ K) and high densities is not very well understood. The cooling rate is expected to be controlled by the combined impact of metal cooling, H^- cooling, and molecular cooling. However, there are not many available tools that can quantify the processes. Therefore, in our analysis using CLOUDY, there are some inherent approximations for the cooling rates. Second, the shock equations were solved using a plane-parallel geometry approximation. In the limit where the region of shocked ionized gas is within ΔR and $\Delta R/R \ll 1$, the approximation is justified to first order.

This is a 1D spherically symmetric model, which has scope for further development. Andrews et al. (2011a) have adopted a bipolar geometry for SN 2010jl in order to simultaneously explain the continuum emission and the optical depths. However, the shock equations deal with microscopic properties of the shocked gas, which are not directly dependent on the geometry of the shell. Therefore, the inferences related to the radiation-induced dust formation drawn in this study remain justified.

We acknowledge NASA's 16-ATP2016-0004 grant for supporting this project. Also, we want to acknowledge the guidance and feedback from Dr. John Raymond, Dr. Jon Slavin, and Dr. Tim Kallman, who have helped us thoroughly during the course of this study. We thank the anonymous referee for the valuable suggestions that have helped us in finalizing the manuscript of this paper.

ORCID iDs

Arkaprabha Sarangi https://orcid.org/0000-0002-9820-679X
Eli Dwek https://orcid.org/0000-0001-8033-1181
Richard G. Arendt https://orcid.org/0000-0001-8403-8548

References

Andrews, J. E., Clayton, G. C., Wesson, R., et al. 2011a, AJ, 142, 45
Andrews, J. E., Sugerman, B. E. K., Clayton, G. C., et al. 2011b, ApJ, 731, 47
Blinnikov, S., Lundqvist, P., Bartunov, O., Nomoto, K., & Iwamoto, K. 2000, ApJ, 532, 1132
Bode, M. F., & Evans, A. 1980, MNRAS, 193, 21P
Bouchet, P., & Danziger, I. J. 1993, A&A, 273, 451
Castor, J. I., Abbott, D. C., & Klein, R. I. 1975, ApJ, 195, 157
Chandra, P., Chevalier, R. A., Chugai, N., Fransson, C., & Soderberg, A. M. 2015, ApJ, 810, 32
Cherchneff, I. 2010, in ASP Conf. Ser. 425, Hot and Cool: Bridging Gaps in Massive Star Evolution, ed. C. Leitherer et al. (San Francisco, CA: ASP), 237
Cherchneff, I., & Dwek, E. 2009, ApJ, 703, 642
Chevalier, R. A. 1982, ApJ, 259, 302
Chugai, N. N. 2009, MNRAS, 400, 866
Chugai, N. N., Blinnikov, S. I., Cumming, R. J., et al. 2004, MNRAS, 352, 1213
Chugai, N. N., & Danziger, I. J. 1994, MNRAS, 268, 173
Chugai, N. N., & Danziger, I. J. 2003, AstL, 29, 649
Clayton, D. D., Liu, W., & Dalgarno, A. 1999, Sci, 283, 1290
Cox, D. P. 1972, ApJ, 178, 143
Cox, D. P., & Raymond, J. C. 1985, ApJ, 298, 651
Dalgarno, A., & McCray, R. A. 1972, ARA&A, 10, 375
Dessart, L., Audit, E., & Hillier, D. J. 2015, MNRAS, 449, 4304

Dessart, L., & Hillier, D. J. 2010, MNRAS, 405, 2141
Draine, B. T., & McKee, C. F. 1993, ARA&A, 31, 373
Draine, B. T., & Salpeter, E. E. 1979, ApJ, 231, 438
Dwarkadas, V. V. 2007, in AIP Conf. Ser. 937, Supernova 1987A: 20 Years After: Supernovae and Gamma-Ray Bursters, ed. S. Immler, K. Weiler, & R. McCray (San Francisco, CA: ASP), 120
Dwek, E. 1983, ApJ, 274, 175
Dwek, E. 1987, ApJ, 322, 812
Dwek, E., & Arendt, R. G. 2008, ApJ, 685, 976
Dwek, E., & Arendt, R. G. 2015, ApJ, 810, 75
Dwek, E., Arendt, R. G., Fox, O. D., et al. 2017, ApJ, 847, 91
Dwek, E., & Cherchneff, I. 2011, ApJ, 727, 63
Fassia, A., Meikle, W. P. S., Chugai, N., et al. 2001, MNRAS, 325, 907
Ferland, G. J., Korista, K. T., Verner, D. A., et al. 1998, PASP, 110, 761
Filippenko, A. V. 1997, ARA&A, 35, 309
Fox, O. D., Chevalier, R. A., Skrutskie, M. F., et al. 2011, ApJ, 741, 7
Fox, O. D., Filippenko, A. V., Skrutskie, M. F., et al. 2013, AJ, 146, 2
Fox, O. D., Van Dyk, S. D., Dwek, E., et al. 2017, ApJ, 836, 222
Fransson, C., Ergon, M., Challis, P. J., et al. 2014, ApJ, 797, 118
Gall, C., Hjorth, J., Watson, D., et al. 2014, Natur, 511, 326
Goumans, T. P. M., & Bromley, S. T. 2012, MNRAS, 420, 3344
Hollenbach, D., & McKee, C. F. 1979, ApJS, 41, 555
Jacobson, M. Z. 2005, Fundamentals of Atmospheric Modeling (2nd ed.; Cambridge: Cambridge Univ. Press)
Jencson, J. E., Prieto, J. L., Kochanek, C. S., et al. 2016, MNRAS, 456, 2622
Kiewe, M., Gal-Yam, A., Arcavi, I., et al. 2012, ApJ, 744, 10
Kotak, R., Meikle, P., van Dyk, S. D., Höflich, P. A., & Mattila, S. 2005, ApJL, 628, L123
Maeda, K., Nozawa, T., Sahu, D. K., et al. 2013, ApJ, 776, 5
Meynet, G., Chomienne, V., Ekström, S., et al. 2015, A&A, 575, A60
Moriya, T. J., Maeda, K., Taddia, F., et al. 2014, MNRAS, 439, 2917
Morris, P. W., Gull, T. R., Hillier, D. J., et al. 2017, ApJ, 842, 79
Nozawa, T., Kozasa, T., Tominaga, N., et al. 2010, ApJ, 713, 356
Ofek, E. O., Arcavi, I., Tal, D., et al. 2014a, ApJ, 788, 154
Ofek, E. O., Rabinak, I., Neill, J. D., et al. 2010, ApJ, 724, 1396
Ofek, E. O., Zoglauer, A., Boggs, S. E., et al. 2014b, ApJ, 781, 42
Pozzo, M., Meikle, W. P. S., Fassia, A., et al. 2004, MNRAS, 352, 457
Sarangi, A., & Cherchneff, I. 2013, ApJ, 776, 107
Sarangi, A., & Cherchneff, I. 2015, A&A, 575, A95
Schlegel, E. M. 1990, MNRAS, 244, 269
Smith, N. 2016, in Handbook of Supernovae, ed. A. W. Alsabti & P. Murdin (Cham: Springer), 403
Smith, N., Chornock, R., Li, W., et al. 2008, ApJ, 686, 467
Smith, N., Silverman, J. M., Filippenko, A. V., et al. 2012, ApJ, 143, 17
Soderberg, A. M., Berger, E., Page, K. L., et al. 2008, Natur, 453, 469
Stoll, R., Prieto, J. L., Stanek, K. Z., et al. 2011, ApJ, 730, 34
Svirski, G., Nakar, E., & Sari, R. 2012, ApJ, 759, 108
Szalai, T., & Vinkó, J. 2013, A&A, 549, A79
Taddia, F., Stritzinger, M. D., Sollerman, J., et al. 2013, A&A, 555, A10
Truelove, J. K., & McKee, C. F. 1999, ApJS, 120, 299
Utrobin, V. P., Wongwathanarat, A., Janka, H.-T., & Müller, E. 2017, ApJ, 846, 37
Veigele, W. J. 1973, AD, 5, 51
Weingartner, J. C., & Draine, B. T. 2001, ApJ, 563, 842
Whalen, D. J., Even, W., Lovekin, C. C., et al. 2013, ApJ, 768, 195
Williams, B. J., & Fox, O. D. 2015, ApJL, 808, L22
Wooden, D. H., Rank, D. M., Bregman, J. D., et al. 1993, ApJS, 88, 477
Zubko, V., Dwek, E., & Arendt, R. G. 2004, ApJS, 152, 211